Condensation on Superhydrophobic Surfaces: The Role of Local Energy Barriers and Structure Length Scale

Citation: Enright, Ryan, Nenad Miljkovic, Ahmed Al-Obeidi, Carl V. Thompson, and Evelyn N. Wang. "Condensation on Superhydrophobic Surfaces: The Role of Local Energy Barriers and Structure Length Scale." Langmuir 28, no. 40 (October 9, 2012): 14424-14432.

As Published: http://dx.doi.org/10.1021/la302599n

Publisher: American Chemical Society (ACS)

Persistent URL: http://hdl.handle.net/1721.1/85003

Version: Author's final manuscript: final author's manuscript post peer review, without publisher's formatting or copy editing

Condensation on superhydrophobic surfaces: The role of local energy barriers and structure length-scale

Ryan Enright[1,2], *Nenad Miljkovic*[1], *Ahmed Al-Obeidi*[1], *Carl V. Thompson*[1], *and Evelyn N. Wang*[1*]

[1]Department of Mechanical Engineering, Massachusetts Institute of Technology, 77 Massachusetts Avenue, Cambridge, Massachusetts, 02139, USA

[2]Stokes Institute, University of Limerick, Limerick, Ireland

ABSTRACT

Water condensation on surfaces is a ubiquitous phase-change process that plays a crucial role in nature and across a range of industrial applications including energy production, desalination, and environmental control. Nanotechnology has created opportunities to manipulate this process through the precise control of surface structure and chemistry, thus enabling the biomimicry of natural surfaces, such as the leaves of certain plant species, to realize superhydrophobic condensation. However, this "bottom-up" wetting process is inadequately described using typical *global* thermodynamic analyses and remains poorly understood. In this work, we elucidate, through imaging experiments on surfaces with structure length scales ranging from 100 nm to 10 μm and wetting physics, how *local* energy barriers are essential to understanding non-equilibrium condensed droplet morphologies and demonstrate that overcoming these barriers *via* nucleation-mediated droplet-droplet interactions leads to the emergence of wetting states not predicted by scale-invariant global thermodynamic analysis.

* Author to whom correspondence should be addressed. enwang@mit.edu

This mechanistic understanding offers insight into the role of surface-structure length-scale, provides a quantitative basis for designing surfaces optimized for condensation in engineered systems, and promises insights into ice formation on surfaces that initiates with the condensation of sub-cooled water.

INTRODUCTION

Understanding the mechanisms governing water condensation on surfaces is crucial to a wide range of applications that have significant societal and environmental impact such as power generation[1], water desalination[2], and environmental control[3]. For example, the thermal efficiency of the steam (Rankine) cycle, which is responsible for the majority of the world's power production, is directly linked to condensation heat-transfer performance[1]. Meanwhile, in HVAC systems, which account for ~10-20% of the total energy consumption in developed countries and are spreading rapidly in emerging economies[3, 4], condensed water accumulating on evaporator coils can lead to degraded performance and the proliferation of pathogens that endanger human health[5, 6]. Water vapor preferentially condenses on solid surfaces rather than directly from the vapor due to the reduced activation energy of heterogeneous nucleation in comparison to homogeneous nucleation[7]. While the excess energy of a surface controls the heterogeneous nucleation process, it also determines the wetting behavior of the condensate which has a significant impact on overall performance. Recently, the use of hydrophobic surfaces structured at capillary length scales has been proposed to enhance heterogeneous condensation[8-20]. Because wetting interactions can be tuned using structure geometry, these surfaces promise a means to manipulate condensation behavior to realize droplet morphologies ranging from highly pinned, *i.e.*, Wenzel state[21], to superhydrophobic, *i.e.*, Cassie state[22], where droplets can shed passively at microscopic length-scales *via* droplet coalescence[9]. However, the effect of surface structure

geometry on condensation behavior remains under debate. A review of previous studies shows that there is a surface-structure length-scale dependency, *i.e.*, microstructures[13, 15, 18] *vs*. nanostructures[8, 9, 16, 20, 23], on the resulting condensed droplet morphology that cannot be readily reconciled using global thermodynamic analyses[24] often used to explain observed condensation behavior[13-15, 18, 25]. This inconsistency highlights a lack of fundamental understanding to explain a "bottom-up" wetting process that begins with the nucleation of droplets with radii on the order of 1 - 10 nm and involves both droplet-surface and droplet-droplet interactions at length-scales ranging from smaller than to larger than the characteristic size of the surface structures.

By studying well-defined structured surfaces spanning a wide range of length scales from 100 nm to 10 μm and functionalized using several hydrophobic thin films, we found that the emergent morphology of isolated droplets interacting with the surface structures during growth is primarily defined by the pinning behavior of the local contact line within the structures. Depending on the relationship between the structure length-scale and the droplet nucleation density, the dominant condensed droplet morphology can then switch to one that is thermodynamically unfavorable in a global sense due to local contact line de-pinning. We show how these isolated condensed droplet morphologies arise by quantitatively describing growth in terms of characteristic local energy barriers and extend this view to explain the role of droplet-droplet interactions in determining emergent droplet morphology. This result contrasts the common macroscopic view of wetting behavior for individual droplets. The understanding of droplet growth behavior developed, coupled with observations indicating that nucleation is initiated by the presence of defects in our hydrophobic thin-films and recent transport modeling[10], provides a rational basis to develop optimized condensing surfaces. This mechanistic framework also has implications for understanding condensation behavior on nature's

superhydrophobic surfaces[26-29] and ice formation on structured surfaces that initiates with the condensation of sub-cooled water[30].

EXPERIMENTAL SECTION

Nanopillars (Fig. 1a) were fabricated by electrodepositing Au from a sodium gold sulfite solution (BDT-510, Ethenone) at a constant current density of 1 mA/cm^2 through a nanoporous anodic alumina (AAO) film[31]. The nanopillars were released by wet etching the AAO template in a 25 wt.% tetramethylammonium hydroxide (TMAH, SACHEM Inc.) solution at 333 K for 2 hours, followed by rinsing in acetone, isopropyl, and deionized (DI) water. After a 30 minute oxygen-plasma clean (Harrick Plasma, Ithaca, NY), the Au samples were immediately immersed in a 2mM 1H,1H,2H,2H-perfluorodecanethiol/ethanol solution (Sigma-Aldrich) for 30 minutes. Upon removal, samples were rinsed with ethanol, DI water, and dried with N_2. Goniometric measurements (MCA-3, Kyowa Interface Science Co., Japan) on a corresponding smooth, thiolated Au surface showed advancing and receding contact angles of $\theta_a = 121.1° \pm 2.2°$ and $\theta_r = 106.3° \pm 2.4°$, respectively.

Silicon nanopillars (Fig. 1b) were fabricated by metal-assisted etching of silicon[32]. Boron doped 1-25 Ω-cm silicon (100) wafers (Silicon Valley Microelectronics, USA) were coated with a trilayer coating consisting of 200 nm thick photoresist film (PFI-88, Sumitomo Chemical Co., Japan), 20 nm SiO_2 via e-beam evaporation, and 300 nm BARLI ARC (AZ Electronic Materials, USA). A Lloyd's mirror set-up ($\lambda = 325$, Helium-Cadmium laser) was utilized to define interference patterns on the resist-SiO_2-ARC trilayer. The photoresist template was transferred into the underlying ARC layer by RIE. Subsequently, a 15 nm Au film was deposited *via* e-beam evaporation. Lift-off of the ARC posts in N-methylpyrrolidone resulted in an anti-dot array which was wet etched in solution consisting of 4.8 M HF and 0.4 M H_2O_2. The Au layer at the

base of the pillars was subsequently removed in an iodine-based etch solution. A range of Si nano and micropillars were also fabricated using standard deep reactive ion etching (DRIE) where the pillar patterns were defined using either e-beam (Fig. 1c) or optical masks (Fig. 1d) and standard projection lithography. See Table 1 for a complete list of pillar geometries fabricated and tested for the study.

Silicon dioxide functionalization was achieved *via* the chemical vapor deposition of either (tridecafluoro-1,1,2,2-tetrahydrooctyl)-1-trichlorosilane (UCT Specialties), octadecyltrichlorosilane (Sigma-Aldrich), or dichlorodimethylsilane (Sigma-Aldrich). The samples were cleaned as described above and then placed in a vacuum chamber containing an open container of silane at room temperature and held at 17.5 kPa for 30 minutes. Upon removal the samples were rinsed in ethanol, DI water, and then dried with N_2. Goniometric measurements on corresponding smooth, silanated silicon surfaces showed advancing and receding contact angles of: $\theta_a/\ \theta_r = 121.6° \pm 1.3°/86.1° \pm 1.3°$; $\theta_a/\ \theta_r = 110.8° \pm 1°/85.8° \pm 0.9°$; and $\theta_a/\ \theta_r = 103.8° \pm 0.5°/102.7° \pm 0.4°$ for deposited films of (tridecafluoro-1,1,2,2-tetrahydrooctyl)-1-trichlorosilane, octadecyltrichlorosilane, and dichlorodimethylsilane, respectively.

Environmental scanning electron microscopy (Zeiss EVO 55 ESEM) was performed in back scatter detection mode with a high gain. The water vapor pressure in the ESEM chamber was 1.4 kPa. Typical image capture was obtained with a beam potential of 20 kV and variable probe current depending on stage inclination angle. A 500 μm lower aperture was used in series with a 1000 μm variable pressure upper aperture for greater detail. Samples were attached using copper tape to a cold stage initially set to a temperature of 285 ± 1.5 K. After equilibrating for 5 minutes, the temperature was decreased to 284 ± 1.5 K resulting in water condensation. Images

and recordings were obtained at an inclination angle of 70° to 80° from the horizontal; at a working distance ranging from 3 to 5 mm. Recordings were performed at 1 fps. To limit droplet heating effects[19] and minimize damage to the functional coatings, probe currents were maintained below 1.9 nA and the view areas were kept above 400 μm x 300 μm.

Optical light microscopy was performed using a custom built set-up described in detail in the Supporting Information (S2). Samples were horizontally-mounted using a thin layer of thermal grease (Omegatherm, Omega) to a cold stage and cooled to the test temperature, typically T_w = 283±0.1 K, in a dry N_2 atmosphere before initiating the flow of water-saturated N_2. The chamber humidity was controlled by adjusting the water reservoir temperature and recorded (Hygroclip, Rotronic) throughout the experiment. Video recordings were performed at 10 fps using a CMOS camera (Phantom v7.1, Vision Research) attached to an upright microscope (Eclipse LV100, Nikon).

We note that both the ESEM and optical experiments were performed at similar thermodynamic and kinetic conditions, *i.e.*, surface temperatures and water vapor pressures. The difference between the experiments was the presence of non-condensable gases (NCGs) in the optical measurements, *i.e.*, N_2. It has been shown that NCGs do not affect the energetics of nucleation[7]. However, NCGs introduce an appreciable diffusion resistance on the gas side that certainly reduces droplet growth rates compared to a pure vapor environment for identical water vapor pressure conditions[7]. Furthermore, NCGs can also play a role in the number of nucleation sites activated due to the depletion of water vapor above the surface, *i.e.*, concentration gradients of water vapor, that are not typically a concern in pure vapor environments. This phenomenon becomes pronounced when the ramp rate to the target supersaturation is small[7]. Accordingly, we adopted the procedure described above for the optical measurements whereby the supersaturation

in the test chamber was rapidly brought to the target value over a timescale of seconds. The efficacy of this approach was confirmed by the observation that the nucleation densities for both the ESEM and optical measurements were of the same order of magnitude for comparable samples. Furthermore, since the presence of NCGs has no effect on the chemical potential of the water vapor, we did not expect the wetting behavior of the growing droplets to be affected by the choice of visualization technique. Indeed, consistent wetting behavior was observed between the two imaging methods.

RESULTS AND DISCUSSION

Individual droplet growth (R ~ l)

We first examined droplet growth during condensation from sizes comparable to a single unit cell, *i.e.,* the space between four pillars, up to the point of coalescence with neighboring droplets using ESEM. Figure 1e & f show two distinct droplet morphologies formed during condensation on two pillar geometries with the same pillar diameter of 300 nm and height of 6.1 μm, but with pitch spacings of $l = 2$ μm and $l = 4$ μm, where the average distance between droplet nucleation sites was $\langle L \rangle \sim 5l$. On both surfaces, droplets were observed to nucleate in a variety of locations with respect to the unit cell, which is consistent with the small size of the critical nucleation radius, $R_c \approx 15$ nm expected for these experimental conditions (see Supporting Information S3).

During ESEM imaging we identified three general growth morphologies: suspended droplets nucleating on the pillar tips that are unconditionally stable in the absence of droplet interactions and forces such as gravity[33]; droplets nucleating on pillar sides that develop pinned contact lines leading to suspended droplet morphologies wetting some portion of the pillars, but

remain unconnected to the base of the pillars; and droplets nucleating within the unit cell which subsequently fill and then grow beyond the unit cell forming either partial wetting Cassie or completely wetting Wenzel morphologies. We studied the last scenario in detail because it is only from this initial condition that the droplet explores the entirety of the structure geometry to fundamentally differentiate between Cassie and Wenzel growth during condensation. This last scenario is also the most promising growth route in terms of maximizing energy transfer rates[10].

Figure 1e shows droplets growing in a partial wetting state that led to nearly spherical morphologies and were weakly pinned to the surface as evidenced by coalescence-induced droplet ejection (see Supporting Movie 1)[14,17]. In contrast, Figure 1f shows droplets that grew and coalesced, but remained in a highly-pinned, fully-wetting state, *i.e.*, coalescence-induced droplet ejection was not observed. The distinct growth behaviors observed in Figs. 1e & f are explained in terms of a *non-equilibrium* energy criterion where contact line pinning plays the determining role in the resulting droplet morphology. By comparing the dimensionless energy for liquid wetting the pillars in the advancing Wenzel[34] ($\cos\theta_a^W = r\cos\theta_a$) and Cassie[35] ($\cos\theta_a^{CB} = -1$) states, the expected droplet morphology can be determined by

$$E^* = \frac{\cos\theta_a^{CB}}{\cos\theta_a^W} = \frac{-1}{r\cos\theta_a}, \qquad (1)$$

where $r = 1 + \pi d r_p h/l^2$ is the surface roughness and r_p ($\approx \pi/2$) is the *local* roughness associated with the scallop features on the pillar sides. Equation (1) implies that when $E^* > 1$, Wenzel droplet morphologies are favoured, while when $E^* < 1$ partially wetting Cassie droplets should emerge. While this criterion is in agreement with the behavior observed in Fig. 1e & f where $E^* = 0.59$ ($r = 3.26$) and $E^* = 1.22$ ($r = 1.56$), respectively, the physical details of the emerging droplet morphology and the role of length scale are not evident.

We investigated the contact line pinning behavior by carefully studying individual growth for droplet radii $R \gtrsim l$ on the surfaces in Fig. 1e & f. Figure 2a (l = 2 μm) shows a representative case where the contact line at the base of the droplet remained pinned within the structures and the droplet grew to resemble the shape of a balloon[12, 19]. The characteristic diameter of the pinned neck for this droplet morphology (5.4 ± 1 μm) indicated a wetted base area spanning ~2 x 2 unit cells (see Supporting Information S4). At later times (t > 4 s in Fig. 2a), these partial wetting droplets had increasingly large apparent contact angles, $\theta_{app} \geq 150°$, characteristic of the Cassie state, reaching values as high as 170° before the onset of coalescence (see Fig. 2c). Conversely, Figures 2b & d (l = 4 μm) show that the droplets underwent a series of de-pinning events resulting in complete wetting of the surface structures. This behavior was accompanied by fluctuations in the apparent contact angle (Fig. 2d) with a value of $\theta_{app} \lesssim 125°$, which was significantly lower than the expected $\theta_a^W = 139.6°$. This discrepancy shows there is a more complex wetting process dictated by contact line pinning behavior of the droplet in the advancing state that is not captured by the Wenzel equation (denominator of equation (1)).

To develop a better understanding of the observed behavior on the two surfaces, we first considered the growth of a droplet just beyond a single unit cell whereby the droplet is bound by energy barriers at the side (ΔE_s) and the top (ΔE_t) of the unit cell. While the exact shape of the meniscus is complex, we determined the initial wetting behavior by estimating and comparing the size of each characteristic energy barrier,

$$E_u^* = \frac{\Delta E_t}{\Delta E_s} = \frac{(r-1)\left(\sqrt{\pi} - 2\sqrt{\varphi}\right)\left(\pi\sqrt{\varphi} - 4\sqrt{\varphi} + 2\sqrt{\pi}\right)}{\pi(1-\varphi)\left(\sqrt{\pi}\sqrt{\varphi}(1-\cos\theta_a) + (r-1) - 2\varphi(1-\cos\theta_a)\right)} \qquad (2)$$

where $\varphi = \pi d^2/4l^2$ is the solid fraction of the pillars (see Supporting Information S5). When the top energy barrier is relatively small ($E_u^* < 1$), the droplet grows above the unit cell, while for $E_u^* > 1$, the droplet favors wetting into neighboring unit cells. This criterion is consistent with the observed behavior in Fig. 2b between t = 1 s and t = 2 s where the droplet was observed to wet into neighboring unit cells ($E_u^* \approx 1.4$) (see also Supporting Figure S5.1). By extending the analysis to a larger number of unit cells, we determined that $E_u^*(n)$ should drop below unity for n = 4 unit cells for the surfaces shown in Figs. 2a & b, which is consistent with the pinned neck diameter demonstrated by the partial wetting Cassie droplets ($E_u^*(4) \approx 0.75$).

Once $\theta_{app} > 90°$ ($E_u^*(n) < 1$), the droplet grows until it reaches a stability limit associated with a characteristic angle α at which the contact line around the perimeter of the wetted unit cells can de-pin and wet downwards towards the base of the pillars (see Fig. 2e). We determined α by considering the local energy requirement for such wetting,

$$\cos\alpha = \sqrt{\pi}\sqrt{\varphi}\, r_p \cos\theta_a + \left(1 - \frac{2\sqrt{\varphi}}{\sqrt{\pi}}\right). \tag{3}$$

Equation 3 is identical to the case of droplet hemi-wicking behavior since in both scenarios the contact line wets a composite surface consisting of solid-vapor and liquid-vapor interfaces (see Supporting Information S6). A further characteristic pinning angle η can be identified when the droplet interface pins to the next row of pillars as

$$\cos\eta = 2\sqrt{\pi}\sqrt{\varphi}\, r_p \cos\theta_a + E_p^*, \tag{4}$$

where E_p^* is a curvature-dependent energy contribution from the pinned contact line in the preceding unit cell that acts to pull the interface down towards the base of the pillars (see Supporting Information S6). In the limit of $R \gg l$, $E_p^* \to \cos\alpha$ or $E_p^* \to \sin\theta_a$, depending on the pinning location of the preceding contact line (see Fig. 2e). Once η is reached the contact line

can de-pin allowing the interface to reach the next row of pillars from which follows $\cos\eta' = 2\sqrt{\pi}\sqrt{\varphi}\, r_p \cos\theta_a + \cos\eta$. This evolution of local energy barriers explains the characteristic balloon-like shape of the partial wetting Cassie morphology observed in Figs. 1e & 2a since a decreasing amount of energy is available to act on the pinned contact line as the droplet interface reaches subsequent rows of pillars.

Based on the predicted initial wetting behavior given by equation (2) and the characteristic pinning angles given by equations (3) and (4), we obtained the evolving apparent contact angle for $R/l > 1$ as shown in Fig. 2c (l = 2 μm). The model shows good agreement with the experimental results, capturing the apparent contact angle at small R/l where we expect $\theta_{app} \to \alpha + 90° \approx 139°$ and two de-pinning events at R/l = 1.64 and R/l = 2.29. Subsequently, we predict a large increase in contact angle that is associated with the contact line remaining pinned until $\theta_{app} = \eta + 90° = 153° - 164°$ (R/l = 4.52 – 7.71). This range of de-pinning angles represents a reasonable bound accounting for curvature effects on E_p^* (see Supporting Information S6). Once the contact line de-pinned, the interface reached the next row of pillars leading to a sharp reduction in the apparent contact angle, $\theta_{app} = 140° - 158°$. Accordingly, due to the weak energy contribution from the previously pinned contact line, $\eta' > 90°$ such that the apparent contact angle tended towards 180° $(\cos\theta_{app} \to -1)$, which is consistent with the numerator of equation (1).

Modeling of the droplet growth behavior in Fig. 2d (l = 4 μm) indicated periodic contact line de-pinning events once $\theta_{app} = \alpha + 90° \approx 123.6°$ for $R/l < 3$. With each de-pinning event, the apparent contact angle relaxed to ~90° as the contact line reached the base of the pillars before the interface could touch the next row of pillars. At later stages of growth ($R/l \geq 3$), the

interface could touch the next row of pillars before the contact line reached the base, but the maximum apparent angle was only slightly larger than $\alpha + 90°$ since in the large curvature limit ($R \sim l$) $E_p^* \approx 1$ (see Supporting Information S6). Thus, in the range of $R/l \lesssim 5$ the model predicted a maximum $\theta_{app} \approx 125°$, which is consistent with the experimentally observed behavior.

Individual droplet growth (R>>l)

To explore the geometric parameters delineating Wenzel and Cassie droplet growth with minimal curvature effects ($R >> l$), we performed a series of condensation experiments using OM on smooth-walled, metal-assisted etched pillar structures ($r_p \approx 1$) with $l \approx 290$ nm (see Fig. 1d). The pitch and diameter of the pillars were held approximately constant with the pillar height and θ_a varied to give a range of $0.1 \leq E^* \leq 3$. During the experiments, the characteristic spacing of nucleated droplets was always $\langle L \rangle > 10l$ and typically $\langle L \rangle \approx 30l$. The wetting state was determined by focusing through the droplets to show light reflecting and light absorbing regions at the surface indicating Cassie and Wenzel wetting, respectively (see Supporting Information S7).

Similar to observations of wetting shapes formed during the spontaneous breakdown of the metastable Cassie state under deposited macroscopic droplets[36], we found that as E^* became larger than unity (decreasing local energy barriers), the wetted area underneath the Wenzel droplets underwent a shape change from approximately square ($E^* \approx 1$) to approaching the limiting case of circular for the shortest pillars ($E^* \to -1/\cos\theta_a$) (see Fig. 3a(ii-iv)) . Close examination of growth near the transition from Cassie to Wenzel growth ($E^* \approx 1$) revealed that

wetting propagated *via* the filling of rows perpendicular to the advancing wetting front of the condensed droplet, *i.e.*, zipping[36] (see Supporting Movie 2).

Interestingly, unlike the case of a macroscopic droplet transitioning from a metastable Cassie state to the Wenzel state, here the dynamics of the wetting process were not limited by viscous dissipation[36], but rather by the rate of condensation to the droplet. This point is highlighted in Fig. 3b, which shows the evolution of θ_{app} with droplet size using ESEM for the surface shown in Fig. 3a(ii). Similar to the behavior observed in Fig. 2d, the droplet approached and then overcame the local energy barriers in a periodic manner. Thus, the observed shape change of the wetted area with increasing E^* was defined exclusively by the characteristic local energy barriers.

Figure 3a shows that (i) the pillars were tall enough such that filling was suppressed and the droplet contact line remained pinned allowing the Cassie state to emerge even in the presence of defects (see Supporting Figure S8), (ii) lowering the pillar height led to wetting where filling normal to the pillar array was energetically favorable resulting in an approximately square wetting shape, (iii) with further lowering of the pillar height filling diagonally to the pillar array became energetically favorable allowing for octagonal wetting shapes, and (iv) for the shortest pillars directional anisotropy in the wetting energy was significantly reduced leading to almost circular wetting shapes.

In order to estimate the energy barrier to filling normal to the pillar array ($\Delta E_{zip,n}$), we considered the pinned interface geometry as a function of the characteristic pinning angles before and after the filling process (see Supporting Information S9). The expression resulting from the analysis is given by,

$$\Delta E_{zip,n} = -\frac{1}{\sqrt{\pi}\sin\theta_a \sin\eta}\Big[([(4\varphi\cos\eta + (r-\varphi)\sin\eta)\cos\theta_a + 1 - \varphi\sin\eta]\sin\theta_a$$
$$- \cos\eta + \cos^2\theta_a\cos\eta)\sqrt{\pi} \qquad (5)$$
$$- 2\sqrt{\varphi}\big((1 - \sin\eta + \pi\cos\theta_a\cos\eta)\sin\theta_a - \cos\eta + \cos^2\theta_a\cos\eta\big)\Big].$$

A similar analysis was performed for the case of diagonal filling (see Supporting Information S9). Equation (5) was consistent with the observations shown in Fig. 3c, which maps the droplet wetting state in terms of the pillar height scaled by the critical pillar height h_{zip} corresponding to $\Delta E^*_{zip,n} = 0$ and equation (1). We found excellent agreement between equation (5) and the experimentally observed transition points from Cassie to Wenzel growth for the three different surface coatings (varying θ_a).This is in contrast to equation (1), which under predicted the transition by as much as 30% for the smallest value of θ_a.

Length-scale-dependent droplet wetting states

In addition to the energy barriers encountered during single droplet growth, droplet coalescence introduces a length-scale dependency on the emergent wetting state when $\langle L\rangle \sim l$ by disrupting the formation of the energy barriers that guide the development of partial wetting Cassie droplets. Figure 4a-d shows condensed droplets on two Cassie-stable surfaces ($E^* < 1$) with significantly different length scales, $l = 0.28$ μm (Au nanopillars) and $l = 12.5$ μm (Si micropillars) captured using OM (see Supporting Movies 3 & 4) and ESEM.

Condensation on the thiolated Au nanopillars resulted in growth of Cassie droplets (Fig. 4a,b) consistent with a calculated $E^* = 0.61 \pm 0.13$. In Fig. 4a, we found that the nucleation density N was $\sim 1/3\times$ the pillar density of the array (l^{-2}) with droplet centres separated by an average distance of $\langle L\rangle = 4.48 \pm 1.16$ μm ($\langle L\rangle / l \approx 16$). Here the droplets grew to a size much larger than the unit cell ($R \gg l$), allowing the local energy barriers to develop before the onset of

coalescence. The merging of two or more droplets typically resulted in coalescence-induced ejection[8, 9]. Following the onset of droplet ejection the average droplet radius became approximately constant at $\langle R \rangle \approx 6$ μm (see Supporting Information S10).

In contrast, condensation on the Si micropillars (Fig. 4c,d) resulted in a nucleation density larger than the density of unit cells, $N > l^{-2}$. In this case, multiple droplets occupied a single unit cell, $\langle L \rangle / l = 0.34 \pm 0.06$. As these droplets grew, they merged with droplets within their unit cell and also in neighbouring unit cells to form liquid films inside the structures (Fig. 4d). After a period of continuing condensation, the films reached the tops of the pillars and subsequently coalesced with droplets nucleating on the pillar tips thereby initiating the formation of Wenzel droplets extending above the pillars. While $E^* = 0.23 \pm 0.01$, the emergence of partially wetting Cassie droplets was not possible because coalescence events bypassed the energy barrier, ΔE_s, associated with individual droplet growth (see equation (2)).

On the basis of these observations, we investigated the coalescence-induced transition from Cassie to Wenzel growth as a function of nucleation density ($\langle L \rangle / l$). This was done by adjusting the supersaturation *S*, defined as the ratio of the vapor pressure to the saturation temperature of the surface, in sequential experiments performed at the same location on a Cassie-stable surface ($l = 4.5$ μm, $E^* = 0.75 \pm 0.04$) (see Supporting Movies 5 & 6). Figure 4e (*S* = 1.55±0.05) shows predominantly Cassie droplet morphologies following the onset of coalescence when $\langle L \rangle / l = 3.54 \pm 2.43$ as confirmed in Fig.4f where a single unit cell under each droplet was wetted ($E_u^*(1) = 0.85$). In contrast, Fig. 4g (*S* = 2.04±0.05) shows that the surface was dominated by irregularly-shaped Wenzel droplets following the onset of coalescence when $\langle L \rangle / l = 2.04 \pm 0.6$.

The existence of a critical droplet separation distance leading to a transition in the emergent wetting state can be understood by considering the pinning behavior of the droplet beyond a single unit cell ($\theta_{app} > 90°$). For the surface in Fig. 4e-h, we calculated $\alpha = 79°(< 90°)$ implying that when coalescence occurred at a separation distance of $2l$ the unit cell in between the droplets was wetted as the contact lines de-pinned during the reconfiguration of the interface (see Supporting Information S11). However, at a larger separation distance of $3l$, wetting of the pillar row separating the two droplets became energetically unfavorable since the *local* energy change required to wet the pillar row was positive,

$\Delta E/\left(\gamma_{lv} l \mathrm{d}x\right) = -2\sqrt{\pi}\sqrt{\varphi}\cos\theta_a - 2\cos\alpha \approx 0.36 > 0$ (see Supporting Information S11).

Regime map & nucleation behavior

Based on the understanding gained concerning the structure-scale dependency on the emergent droplet morphology, a regime map was developed defining a parametric space with the experimentally measured $\langle L\rangle/l$ ratios and calculated E^* (see Fig. 5a). Since droplet separation distances were not uniform and demonstrated some variability about the mean, a mixture of Cassie and Wenzel wetting modes can emerge as $\langle L\rangle/l$ becomes greater than unity in the region where $E^* \lesssim 1$. When $\langle L\rangle/l \gtrsim 2-5$ (with the precise value depending on E_u^* and α) and $E^* \lesssim 1$ the formation of partial wetting Cassie droplets is favoured, while when $\langle L\rangle/l$ is below the critical value Wenzel droplets form irrespective of the energetically preferred wetting state because the resulting morphology is dictated by droplet-droplet interactions. Note, the global droplet morphology can be comprised of a mixture of partial wetting and suspended droplets (see Fig. 1a) that can coalesce at separation distances smaller than those required to prevent a Wenzel transition between two coalescing, partial wetting droplets. Furthermore, while the stable region

for Cassie growth is defined more accurately by the row filling energy barrier, equation (5), in the limit as $\langle L \rangle / l \gg 1$, E^* nonetheless serves as a conservative and simple estimate of the preferred wetting state.

The regime map highlights the key role of nucleation density, which determines $\langle L \rangle$, on the emergent droplet morphology for $E^* < 1$. To characterize the nucleation phenomenon, a series of experiments were performed using OM to determine the density and distribution of nucleated droplets on a range of surface geometries. The nucleation site distribution followed Poisson statistics suggesting a spatially random process (see Fig. 5b). While this result appears consistent with a stochastic nucleation process on a homogenous substrate, the observed critical supersaturation ($S_c \approx 1 - 1.1$) was not consistent with classic nucleation theory, which predicts $S_c > 2.75$ for the surface coatings tested (see Supporting Information S12). The observed discrepancy indicated the presence of randomly-distributed, high-surface-energy nucleation sites on the surfaces[37].

The nature of these sites was investigated by studying the distribution of condensed droplets on re-deposited silane films (SAM) at a fixed spatial location on a structured surface (see Fig. 5c). The results showed a direct correlation between the distribution of nucleation sites and the deposited SAM suggesting the significant role of SAM defects in initiating the phase transition. The formation of SAM defects during deposition is well known[38-40] and stable water nanodroplets at ambient conditions have recently been observed at SAM defect sites on the exposed high-surface-energy substrate[41]. Indeed, during ESEM imaging we found that it was possible to use the electron beam to induce damage in the SAM to locally increase the nucleation density *in situ* (see Supporting Information S12). It would be interesting to explore techniques that can controllably introduce nanoscale nucleation sites onto structured surfaces in order to

maximize heat transfer performance or that can produce surfaces with a minimum of nucleation sites to modify the behavior of surface icing initiated from the condensation of sub-cooled water.

CONCLUSIONS

We have presented a mechanistic framework to explain the complex nature of water condensation on structured surfaces which defines *local* energy barriers as key to understanding the growth process and identifies the role of nucleation density on the emergent droplet morphology. We found that the *local* energy barriers can be quantified by addressing the energy requirements for local contact line de-pinning rather than those associated with the global droplet view. This local view of the wetting process was highlighted in the regime where $R/l >> 1$, showing that the Wenzel wetting state propagates via zipping in a manner identical to the breakdown of the Cassie Baxter state for macroscopic droplets. A model for this behavior was developed using characteristic local energy barriers and showed excellent agreement with experiments. The role of length scale in determining the emergent wetting state was found to be dictated by the droplet nucleation density and was successfully explained in terms of local contact line de-pinning behavior during droplet coalescence. Nucleation behavior at low supersaturations was found to be linked to the thin-films used to functionalize the otherwise hydrophilic surfaces, which suggests that engineering of these films could allow surfaces to be optimized in terms of structure scale and nucleation density to provide a further level of control over the phase change process. The findings have significant relevance to the application of structurally-enhanced condensation surfaces.

References

1. Beér, J. M., High efficiency electric power generation: The environmental role. *Progress in Energy and Combustion Science* **2007,** *33* (2), 107-134.
2. Khawaji, A. D.; Kutubkhanah, I. K.; Wie, J. M., Advances in seawater desalination technologies. *Desalination* **2008,** *221* (1-3), 47-69.
3. Pérez-Lomabard, L.; Ortiz, J.; Pout, C., A review on buildings energy consumption information *Energy and Buildings* **2008,** *40* (3), 394-398.
4. Li, B.; Yao, R., Urbanisation and its impact on building energy consumption and efficiency in China. *Renewable Energy* **2009,** *34* (9), 1994-1998.
5. Kim, M. H.; Bullard, C. W., Air-side performance of brazed aluminium heat exchangers under dehumidifying conditions. *International Journal of Refrigeration* **2002,** *25* (7), 924-934.
6. Hugenholtz, P.; Fuerst, J. A., Heterotropic bacteria in air-handling system. *Appl. Environ. Microbiol.* **1992,** *58* (12), 3914-3920.
7. Kashchiev, D., *Nucleation: Basic Theory with Applications*. 1 ed.; Butterworth-Heinemann: Oxford, 2000.
8. Chen, C.-H.; Cai, Q.; Tsai, C.; Chen, C.-L.; Xiong, G.; Yu, Y.; Ren, Z., Dropwise condensation on superhydrophobic surfaces with two-tier roughness. *Appl. Phys. Lett.* **2007,** *90* (17), 173108.
9. Boreyko, J. B.; Chen, C.-H., Self-propelled dropwise condensate on superhydrophobic surfaces. *PRL* **2009,** *103* (18), 184501.
10. Miljkovic, N.; Enright, R.; Wang, E. N., Effect of droplet morphology on growth dynamics and heat transfer during condensation on superhydrophobic nanostructured surfaces. *ACS Nano* **2012,** *6* (2), 1776-1785.
11. Rykaczewski, K.; Scott, J. H. J.; Rajauria, S.; Chinn, J.; Chinn, A. M.; Jones, W., Three dimensional aspects of droplet coalescence during dropwise condensation on superhydrophobic surfaces. *Soft Matter* **2011,** *7*, 8749-8752.
12. Rykaczewski, K.; Scott, J. H. J., Methodology for imaging nano-to-microscale water condensation dynamics on complex nanostructures. *ACS Nano* **2011,** *5* (7), 5962-5968.
13. Dorrer, C.; Rühe, J., Condensation and wetting transitions on microstructured ultrahydrophobic surfaces. *Langmuir* **2007,** *23*, 3820.
14. Narhe, R. D.; Beysens, D. A., Growth dynamics of water drops on a square-pattern rough hydrophobic surface. *Langmuir* **2007,** *23* (12), 6486-6489.
15. Wier, K. A.; McCarthy, T. J., Condensation on ultrahydrophobic surfaces and its effect on droplet mobility: ultrahydrophobic surfaces are not always water repellant. *Langmuir* **2006,** *22*, 2433.
16. Dorrer, C.; Rühe, J., Wetting of silicon nanograss: from superhydrophilic to superhydrophobic surfaces. *Adv. Mater.* **2008,** *20* (1), 159-163.
17. Dietz, C.; Rykaczewski, K.; Fedorov, A. G.; Joshi, Y., Visualization of droplet departure on a superhydrophobic surface and implications to heat transfer enhancement during dropwise condensation. *Appl. Phys. Lett.* **2010,** *97*, 033104.
18. Narhe, R. D.; Beysens, D. A., Nucleation and growth on a superhydrophobic grooved surface. *Phys. Rev. Lett.* **2004,** *93* (7), 076103.
19. Rykaczewski, K.; Scott, J. H. J.; Fedorov, A. G., Electron beam heating effects during environmental scanning electron microscopy imaging of water condensation on superhydrophobic surfaces. *Appl. Phys. Lttrs.* **2011,** *98*, 093106.
20. X. Chen, J. W., R. Ma, M. Hua, N.Koratkar, S. Yao, Z. Wang, Nanograssed micropyramidal architectures for continuous dropwise condensation. *Adv. Funct. Mater.* **2011,** *21* (24), 4617-4623.
21. Wenzel, R., Resistance of solid surfaces to wetting by water. *Ind. Eng. Chem.* **1936,** *28* (8), 988-994.
22. Cassie, A. B. D.; Baxter, S., Wettability of porous surfaces. *Trans. Faraday Soc.* **1944,** *40*, 546-551.

23. Lau, K. K. S.; Bico, J.; Teo, K. B. K.; Chhowalla, M.; Amaratunga, G. A. J.; Milne, W. I.; McKinley, G. H.; Gleason, K. K., Superhydrophobic carbon nanotube forests. *Nano Lett.* **2003,** *3* (null), 1701.
24. Quéré, D., Wetting and Roughness. *Annual Review of Materials Research* **2008,** *38* (1), 71-99.
25. Rykaczewski, K.; Osborn, W. A.; Chinn, J.; Walker, M. L.; Scott, J. H. J.; Jones, W.; Hao, C.; Yao, S.; Wang, Z., How nanorough is rough enough to make a surface superhydrophobic during water condensation? *Soft Matter* **2012,** *8*, 8786.
26. Mockenhaupt, B.; Ensikat, H.-J. r.; Spaeth, M.; Barthlott, W., Superhydrophobicity of biological and technical surfaces under moisture condensation: stability in relation to surface structure. *Langmuir* **2008,** *24* (23), 13591-13597.
27. Cheng, Y. T.; Rodak, D. E., Is the lotus leaf superhydrophobic? *Appl. Phys. Lett.* **2005,** *86*, 144101.
28. Cheng, Y. T.; Rodak, D. E.; Angelopoulos, A.; Gacek, T., Microscopic observations of condensation of water on lotus leaves. *Appl. Phys. Lett.* **2005,** *87*, 194112.
29. Zheng, Y.; Han, D.; Zhai, J.; Jiang, L., *In situ* investigation on dynamic suspending of microdroplet on lotus leaf and gradient of wettable micro- and nanostructure from water condensation. *Appl. Phys. Lett.* **2008,** *92*, 084106.
30. Meuler, A. J.; McKinley, G. H.; Cohen, R. E., Exploiting topological texture to impart icephobicity. *ACS Nano* **2010,** *4* (12), 7048-7052.
31. Oh, J.; Shin, Y. C.; Thompson, C. V., A tungsten interlayer process for fabrication of through-pore AAO scaffolds on gold substrates. *J. Electrochem. Soc.* **2011,** *158* (1), K11-K15.
32. Chang, S. W.; Chuang, V. P.; Boles, S. T.; Ross, C. A.; Thompson, C. V., Densely-packed arrays of ultrahigh-aspect-ratio silicon nanowire fabricated using block copolymer lithography and metal-assisted etching. *Adv. Funct. Mater.* **2009,** *19*, 2495-2500.
33. Oliver, J. F.; Huh, C.; Mason, S. G., Resistance to spreading of liquids by sharp edges. *J. Colloid Interface Sci.* **1977,** *59*, 568.
34. Lafuma, A.; Quere, D., Superhydrophobic states. *Nature Mater.* **2003,** *2* (7), 457-460.
35. Choi, W.; Tuteja, A.; Mabry, J. M.; Cohen, R. E.; McKinley, G. H., A modified Cassie-Baxter relationship to explain contact angle hysteresis and anisotropy on non-wetting textured surfaces. *J. Colloid Interface Sci.* **2009,** *339*, 208-216.
36. Sbragaglia, M.; Peters, A. M.; Pirat, C.; Borkent, B. M.; Lammertink, R. G. H., Spontaneous breakdown of superhydrophobicity. *Phys. Rev. Lett.* **2007,** *99*, 156001.
37. McCormick, J. L.; Westwater, J. W., Nucleation sites for dopwise condensation. *Chem. Eng. Sci.* **1965,** *20*, 1021-1036.
38. Love, J. C.; Estroff, L. A.; Kriebel, J. K.; Nuzzo, R. G.; Whitesides, G. M., Self-Assembled Monolayers of Thiolates on Metals as a Form of Nanotechnology. *Chem. Rev.* **2005,** *105* (4), 1103-1170.
39. López, G. P.; Biebuyck, H. A.; Frisbie, C. D.; Whitesides, G. M., Imaging of features on surfaces by condesation figures. *Science* **1993,** *260* (5108), 647-649.
40. Mandler, D.; Turyan, I., Applications of self-assembled monolayers in electroanalytical chemistry. *Electroanalysis* **1996,** *8* (3), 207-213.
41. Cao, P.; Xu, K.; Varghese, J. O.; Heath, J. R., The microscopic structure of adsorbed water on hydrophobic surfaces under ambient conditions. *Nano Lett.* **2011,** *dx.doi.org/10.1021/nl2036639*.

Acknowledgements: R.E. acknowledges funding received from the Irish Research Council for Science, Engineering, and Technology, cofunded by Marie Curie Actions under FP7. N.M. and

E.N.W. acknowledge funding support from the MIT S3TEC Center, an Energy Frontier Research Center funded by the Department of Energy, Office of Science, Office of Basic Energy Sciences. This work was performed in part at the Center for Nanoscale Systems (CNS), a member of the National Nanotechnology Infrastructure Network (NNIN), which is supported by the national Science Foundation under NSF award no. ECS-0335765. CNS is part of Harvard University.

Supporting Information Six videos showing characteristic condensed droplet behavior on the structured surfaces, as well as further information detailing data collection methodology, nucleation calculations and derivation of local wetting energy barriers. This material is available free of charge via the Internet at http://pubs.acs.org..

Corresponding Author

* Author to whom correspondence should be addressed. enwang@mit.edu

Figure legends

Figure 1 Fabricated surfaces and global droplet morphologies. a-d Scanning electron micrographs of fabricated pillar geometries spanning a range of length scales from 100 nm to 10 μm. **a** Electrodeposited Au nanopillars defined by an anodic alumina template. Scale bar: 200 nm. **b** Si nanopillars fabricated using interference lithography and metal-assisted wet etching. Scale bar: 500 nm. **c** Si nanopillars fabricated using e-beam written mask and DRIE. Scale bar: 1 μm. **d** Si micropillars fabricated using optical lithography and DRIE. Scale bar: 10 μm. Condensed droplet growth observed using ESEM on surfaces similar to **c** with **e** Cassie droplets where $l = 2$ μm (Reprinted with permission from Miljkovic, Enright and Wang, *ACS Nano*, 2012, 6 (2), 1776. Copyright 2012 American Chemical Society.) and **f** Wenzel droplets where $l = 4$ μm. The diameter and height of the pillars were $d = 300$ nm and $h = 6.1$ μm. The surfaces were functionalized with a silane having an intrinsic advancing contact angle of $\theta_a \approx 122°$ (see Methods). Nucleation conditions: $T_w = 284 \pm 1.5$ K and $S = 1.07 \pm 0.11$. Scale bars: 60 μm.

Figure 2 Evolution of individual droplet morphology. Time-lapse images of individual condensed droplets on structured surfaces showing the progression of **a** partial wetting Cassie ($E^* = 0.57 \pm 0.05$) and **b** Wenzel ($E^* = 1.22 \pm 0.06$) growth. The pillar geometry was $d = 300$ nm and $h = 6.1$ μm (Fig. 1e) with pitch spacings of **a** $l = 2$ μm and **b** $l = 4$ μm. The scallop features on the pillar sides were accounted for as $h' = r_f h$ in the calculation of r. Nucleation conditions: $T_w = 284 \pm 1.5$ K and $S = 1.07 \pm 0.11$. Scale bars: 10 μm. Measured apparent contact angles (○) as a function of R/l for **c** $l = 2$ μm and **d** $l = 4$ μm. In **c** and **d**, (●) correspond to the droplets in **a** and **b**, respectively. The solid line shows the predicted contact angle behavior using the developed model. Uncertainty bars were determined from the propagation of error associated with measurement of the droplet dimensions. Schematics of the droplet pinned contact line showing the evolution from **e** a single unit cell defined by α and η to **f** multiple unit cells defined by α, η and η'.

Figure 3 Cassie to Wenzel droplet growth transition during condensation. The pitch and diameter of the pillars were held approximately constant at $l \approx 300$ nm and $d \approx 110$ nm ($\varphi \approx 0.11$), while the pillar height was varied from 37 nm to 1.77 μm ($1.2 \leq r \leq 8.2$). **a** OM images with false coloring showing the wetted area underneath droplets observed by focusing through the droplets to reveal the wetting state and project the shape of the contact line ($\theta_a \approx 122°$). Scale bar: (i) 10 μm, (ii) - (iv) 20 μm. **b** Apparent contact angles measured using ESEM corresponding to **a**(ii). The dashed line shows $\eta = \cos^{-1}\left(2\sqrt{\pi}\sqrt{\varphi}\cos\theta_a + \sin\theta_a\right) = 166.4°$, while the solid line shows $\theta_a^W = 146.8°$. Uncertainty bars were determined from the propagation of error associated with measurement of the droplet dimensions. **c** Functional wetting state of condensed droplets defined as Cassie (solid symbols) and Wenzel (open symbols) for $\theta_a \approx 122°$ (○), $\theta_a \approx 111°$ (□), and $\theta_a \approx 104°$ (△). Uncertainty bars were determined from the propagation of error associated with measurement of the structure geometry and contact angles. OM nucleation conditions: $T_w = 283 \pm 0.1$ K and $S = 1.5$ - 1.7. ESEM nucleation conditions: $T_w = 284 \pm 1.5$ K and $S = 1.07 \pm 0.11$.

Figure 4 Coalescence-induced transition. Images of droplet growth on **a, b** Au nanopillars ($E^* = 0.61 \pm 0.13$, Fig. 1c) and **c, d** Si micropillars ($E^* = 0.27 \pm 0.01$, Fig. 1f) obtained using **a, c** OM

($T_w = 283 \pm 0.1$ K and $S = 1.78 \pm 0.05$) and **b, d** ESEM ($T_w = 284 \pm 1.5$ K and $S = 1.07 \pm 0.11$). The arrow in **d** indicates a wetting morphology formed via coalescence of droplets in neighboring unit cells. OM scale bars: **a** 30 μm and **c** 20 μm. ESEM scale bars: **b** 40 μm and **d** 60 μm. In **e-h** condensation behavior on a microstructured surface ($l = 4.5$ μm, $d = 2$ μm, $h = 5$ μm, $E^* = 0.75 \pm 0.04$) is shown at a fixed location. In **e, f** the nucleation conditions are $T_w = 283 \pm 0.1$ K and $S = 1.55 \pm 0.05$ ($R_c = 2.6 \pm 0.2$ nm) resulting in a nucleation density of $N = 8.25 \times 10^8$ m^{-2} and a scaled coalescence length of $\langle L \rangle / l = 3.54 \pm 2.43$. In **e** the focal plane is ~30 μm above the pillar tops. The resulting droplet morphology is consistent with the partial wetting Cassie state as shown in **f** where focusing through the droplets reveals a single wetted unit cell ($E_u^*(1) = 0.85$). In **g, h** the nucleation conditions are $T_w = 283 \pm 0.1$ K and $S = 2.04 \pm 0.05$ ($R_c = 1.6 \pm 0.1$ nm) resulting in a nucleation density of $N = 5 \times 10^9$ m^{-2} and a scaled coalescence length of $\langle L \rangle / l = 2.04 \pm 0.6$. The resulting droplet morphology is consistent with the Wenzel state displaying pinned, irregular drop shapes. In **h** transition to a Wenzel state is observed for coalescing droplets separated by $L/l = 2$. Scale bars: **e, g** 50 μm, **f** 30 μm and **h** 15 μm.

Figure 5 Droplet morphology regime map and nucleation behavior. a Regime map characterizing the dominant wetting behavior observed during condensation with coordinates of $\langle L \rangle / l$ and E^*. Cassie morphologies (□) emerge at large $\langle L \rangle / l$ and $E^* \lesssim 1$ (shaded region). Wenzel morphologies (○) emerge at low $\langle L \rangle / l$ and/or $E^* \gtrsim 1$. The horizontal uncertainty bars were determined from the propagation of error associated with measurement of the structure geometry and θ_a. The vertical error bars represent one standard deviation in the mean separation distance between droplets. **b** Measured mean separation distances between droplet centers for a range of samples where $\langle L \rangle / l > 1$ are shown in comparison to the Poisson distribution (solid line), which predicts a mean separation distance $L_p = (1/2)N^{-1/2}$, and for a uniform distribution (dashed line), $L_{ud} = N^{-1/2}$. Error bars represent one standard deviation. **c** Nucleation behavior on a structured silicon surface ($l = 3.5$ μm) for two different CVD silane films at a fixed location, C1 (□) & C2 (△). The nucleation sites for each coating ($n_{C1} = 247$, $n_{C2} = 263$) were repeatable as shown by the deviation of the cumulative probability distribution from the predicted Poisson behavior, $P = 1 - e^{-N\pi L^2}$. An overlay of the nucleation sites observed for C1 and C2 ($n_{C1+C2} = 151$) (○) were found to conform closely to the Poisson distribution (solid line).

Superhydrophobic condensation: The role of length scale and energy barriers

March 10, 2012

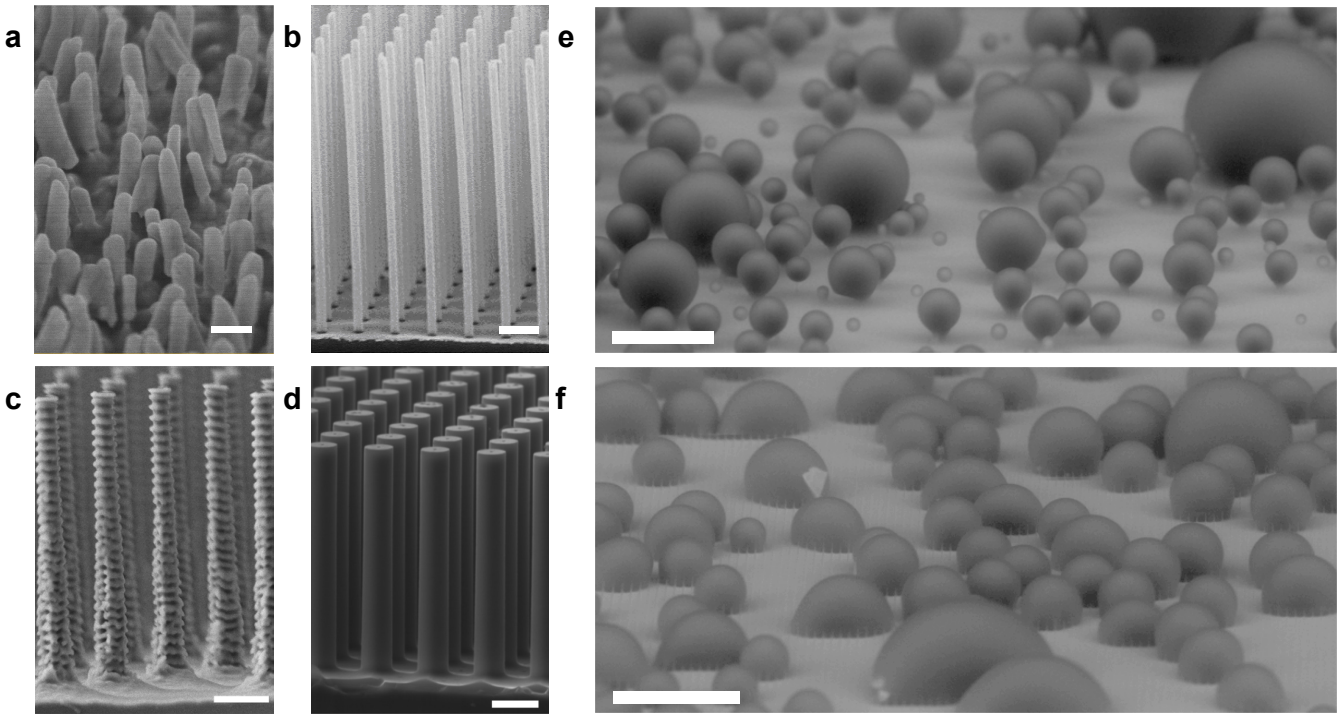

Figure 1: **Fabricated surfaces and global droplet morphologies.** (a-d) Scanning electron micrographs of fabricated pillar geometries spanning a range of length scales from 100 nm to 10 µm. Each surface was characterized by a unique solid fraction $\phi = \pi d^2/4l^2$ and roughness $r = 1+\pi dh/l^2$, where l is the centre-to-centre pillar spacing (pitch), d is the pillar diameter, and h is the pillar height. (a) Electrodeposited Au nanopillars defined by an anodic alumina template. Scale bar: 200 nm. (b) Si nanopillars fabricated using interferance lithography and metal-assisted wet etching. Scale bar: 500 nm. (c) Si nanopillars fabricated using e-beam lithography and DRIE. Scale bar: 1 µm. (d) Si micropillars fabricated using optical lithography and DRIE. Scale bar: 10 µm. Condensed droplet growth observed using ESEM on surfaces similar to (c) with (e) Cassie droplets where $l = 2$ µm and (f) Wenzel droplets where $l = 4$ µm. The diameter and height of the pillars were $d = 0.3$ nm and $h = 6.1$ µm. The scallop features on the pillar sides were characterized as $r_p = \pi/2$. The surfaces were functionalized with a silane having a intrinsic advancing contact angle of $\theta_a \approx 122°$(see Methods). Nucleation conditions: $T_w = 284 \pm 1.5$ K and $S = 1.07 \pm 0.11$. Scale bars: 60 µm.

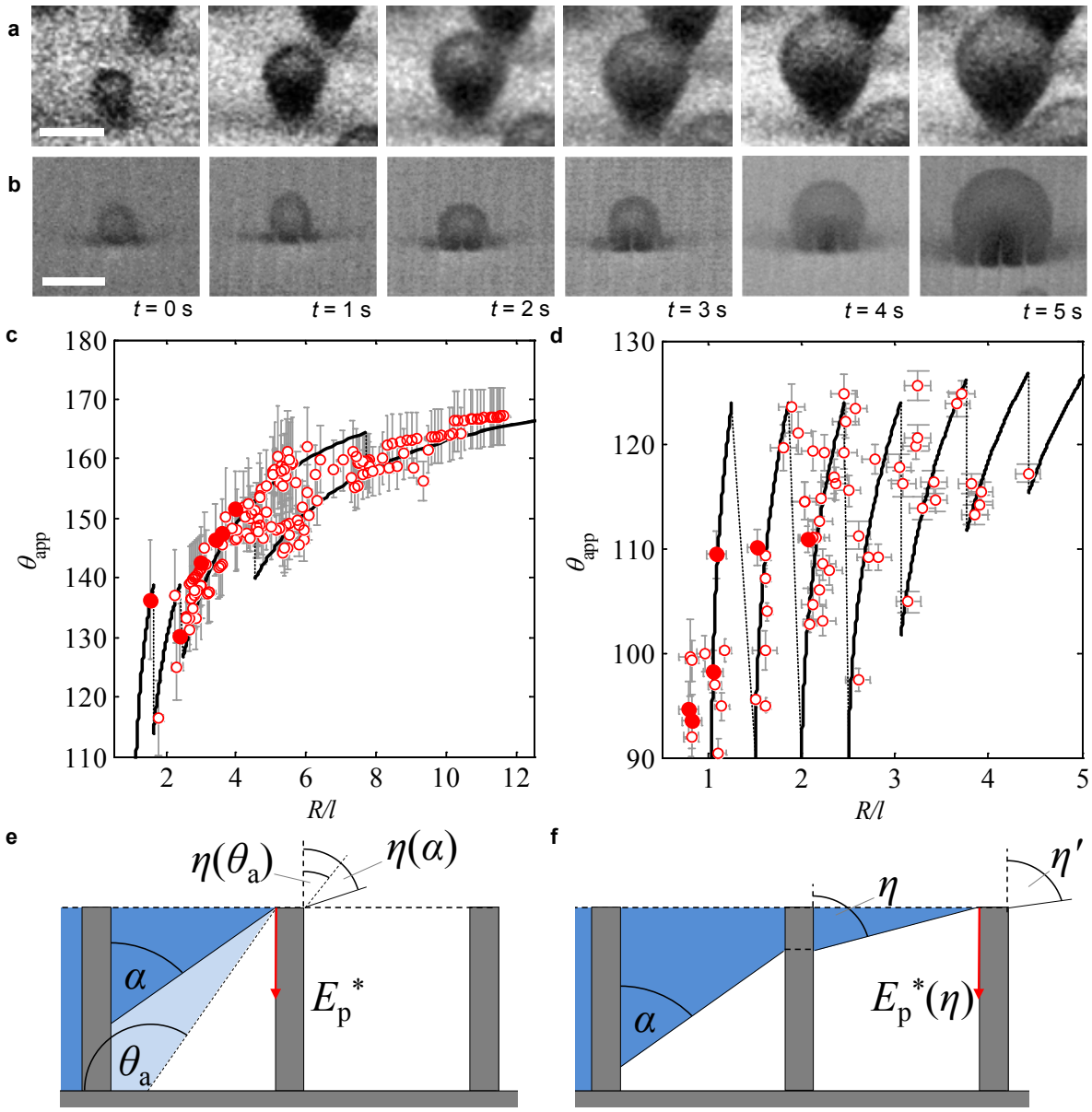

Figure 2: **Evolution of individual droplet morphology.** Time-lapse images of individual condensed droplets on structured surfaces showing the progression of (a) partial-wetting Cassie ($E^* = 0.57 \pm 0.05$) and (b) Wenzel ($E^* = 1.22 \pm 0.06$) growth. The pillar geometry was $d = 300$ nm and $h = 6.1$ µm (Fig. 1e) with pitch spacings of (a) $l = 2$ µm and (b) $l = 4$ µm. The scallop features on the pillar sides were accounted for as $h' = r_p h$ in the calculation of r. Nucleation conditions: $T_w = 284 \pm 1.5$ K and $S = 1.07 \pm 0.11$. Scale bars: 10 µm. Measured apparent contact angles (○) as a function of R/l for (c) $l = 2$ µm and (d) $l = 4$ µm. In (c) and (d), (●) correspond to the droplets in (a) and (b), respectively. The solid line shows the predicted contact angle behaviour using the developed model. Uncertainty bars were determined from the propagation of error associated with measurement of the droplet dimensions. Schematics of the droplet pinned contact line showing the evolution from (e) a single unit cell defined by α and η to (f) multiple unit cells defined by α, η and η'.

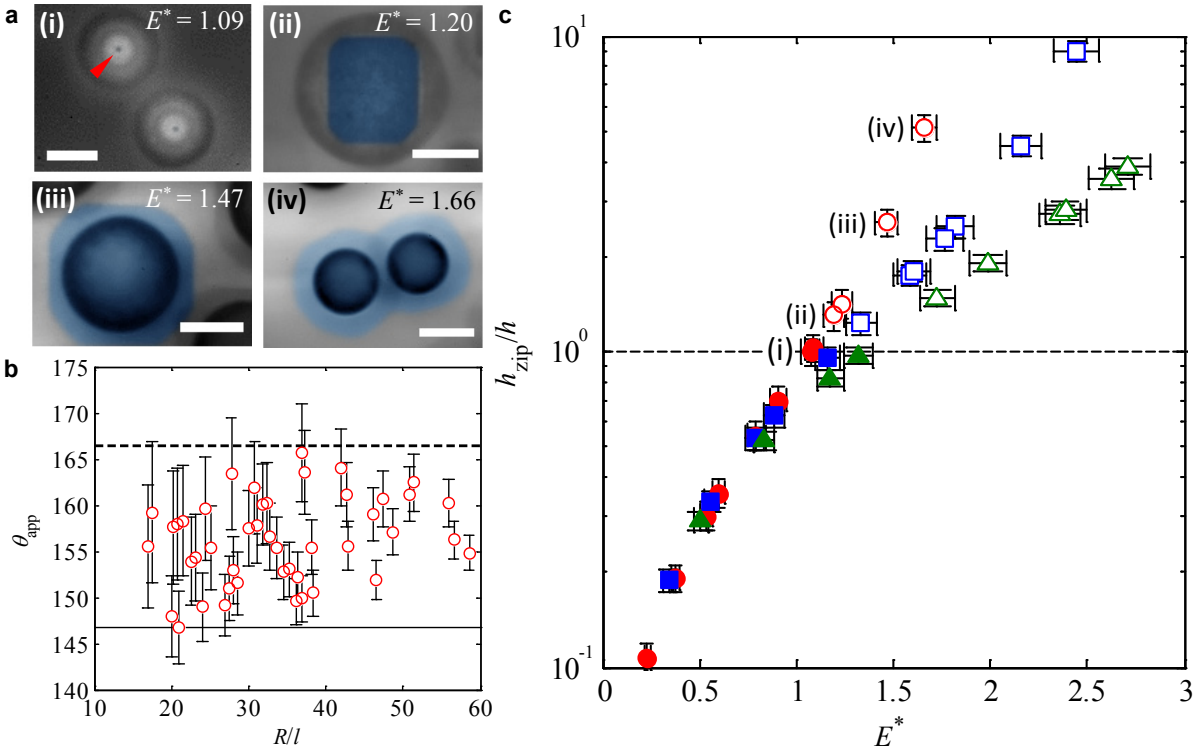

Figure 3: **Cassie to Wenzel droplet growth transition during condensation.** The pitch and diameter of the pillars were held approximately constant at $l \approx 300$ nm and $d \approx 110$ nm ($\phi \approx 0.11$), while the pillar height was varied from 37 nm to 1.77 μm ($1.2 \leq r \leq 8.2$). (a) OM images with false colouring showing the wetted area underneath droplets observed by focusing through the droplets to reveal the wetting state and project the shape of the contact line ($\theta_a \approx 122°$). Scale bar: (i) 10 μm, (ii) - (iv) 20 μm. (b) Apparent contact angles measured using ESEM corresponding to (a, ii). The dashed line shows the calculated $\eta = \cos^{-1}\left(2\sqrt{\pi}\sqrt{\phi}\cos\theta_a + \sin\theta_a\right) = 166.4°$, while the solid line shows $\theta_a^W = 146.8°$. Uncertainty bars were determined from the propagation of error associated with measurement of the droplet dimensions. (c) Functional wetting state of condensed droplets defined as Cassie (solid symbols) and Wenzel (open symbols) for $\theta_a \approx 122°$(○), $\theta_a \approx 111°$(□) and $\theta_a \approx 104°$(△). Uncertainty bars were determined from the propagation of error associated with measurement of the structure geometry and contact angles. OM nucleation conditions: $T_w = 284 \pm 0.1$ K and $S = 1.5 - 1.7$. ESEM nucleation conditions: $T_w = 284 \pm 1.5$ K and $S = 1.07 \pm 0.11$.

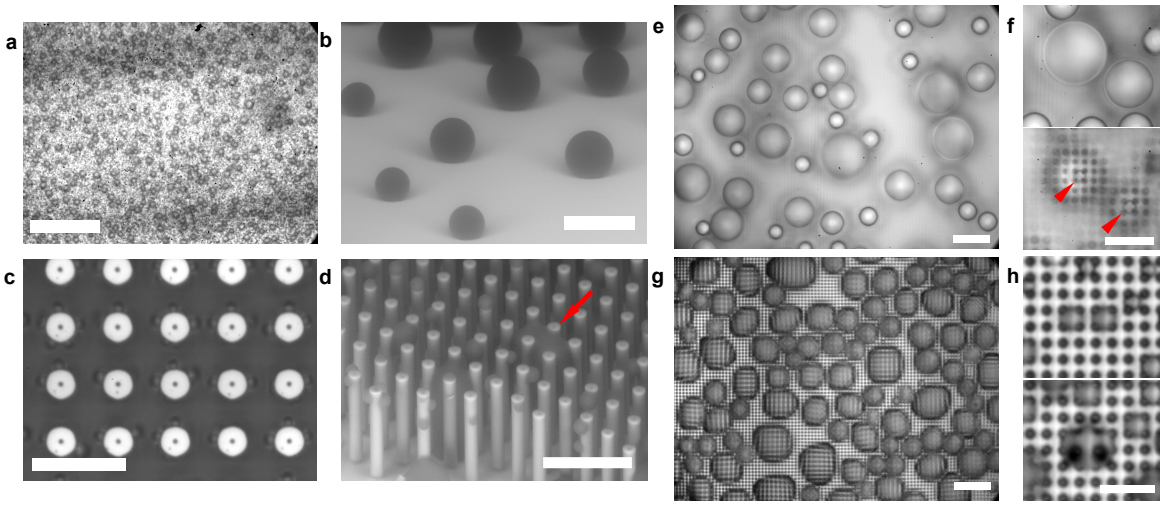

Figure 4: **Coalescence-induced transition.** Images of droplet growth on (a, b) Au nanowires ($E^* = 0.61 \pm 0.13$, Fig. 1c) and (c, d) Si micropillars ($E^* = 0.27 \pm 0.01$, Fig. 1f) obtained using (a, c) OM ($T_w = 283 \pm 0.1$ K and $S = 1.78 \pm 0.05$) and (b, d) ESEM ($T_w = 284 \pm 1.5$ K and $S = 1.07 \pm 0.11$). OM scale bars: (a) 30 µm and (c) 20 µm. ESEM scale bars: (b) 40 µm and (d) 60 µm. In (e-h) condensation behavior on a microstructured surface ($l = 4.5$ µm, $d = 2$ µm, $h = 5$ µm, $E^* = 0.75 \pm 0.04$) is shown at a fixed location. In (e, f) the nucleation conditions are $T_w = 283 \pm 0.1$ K and $S = 1.55 \pm 0.05$ ($R_c = 2.6 \pm 0.2$ nm) resulting in a nucleation density of $N = 8.25x10^8 \mathrm{m}^{-2}$ and a scaled coalescence length of $\langle L \rangle / l = 3.54 \pm 2.43$. In (e) the focal plane is ~30 µm above the pillar tops. The resulting droplet morphology is consistent with the partial wetting Cassie state as shown in (f) where focusing through the droplets reveals a single wetted unit cell ($E_u^*(1) = 0.85$). In (g, h) the nucleation conditions are $T_w = 283 \pm 0.1$ K and $S = 2.04 \pm 0.05$ ($R_c = 1.6 \pm 0.1$ nm) resulting in a nucleation density of $N = 5x10^9 \mathrm{m}^{-2}$ and a scaled coalescence length of $\langle L \rangle / l = 2.04 \pm 0.6$. The resulting droplet morphology is consistent with the Wenzel state displaying pinned, irregular drop shapes. In (h) transition to a Wenzel state is observed for coalescing droplets separated by $L/l = 2$. Scale bars: (e, g) 50 µm, (f) 30 µm and (h) 15 µm.

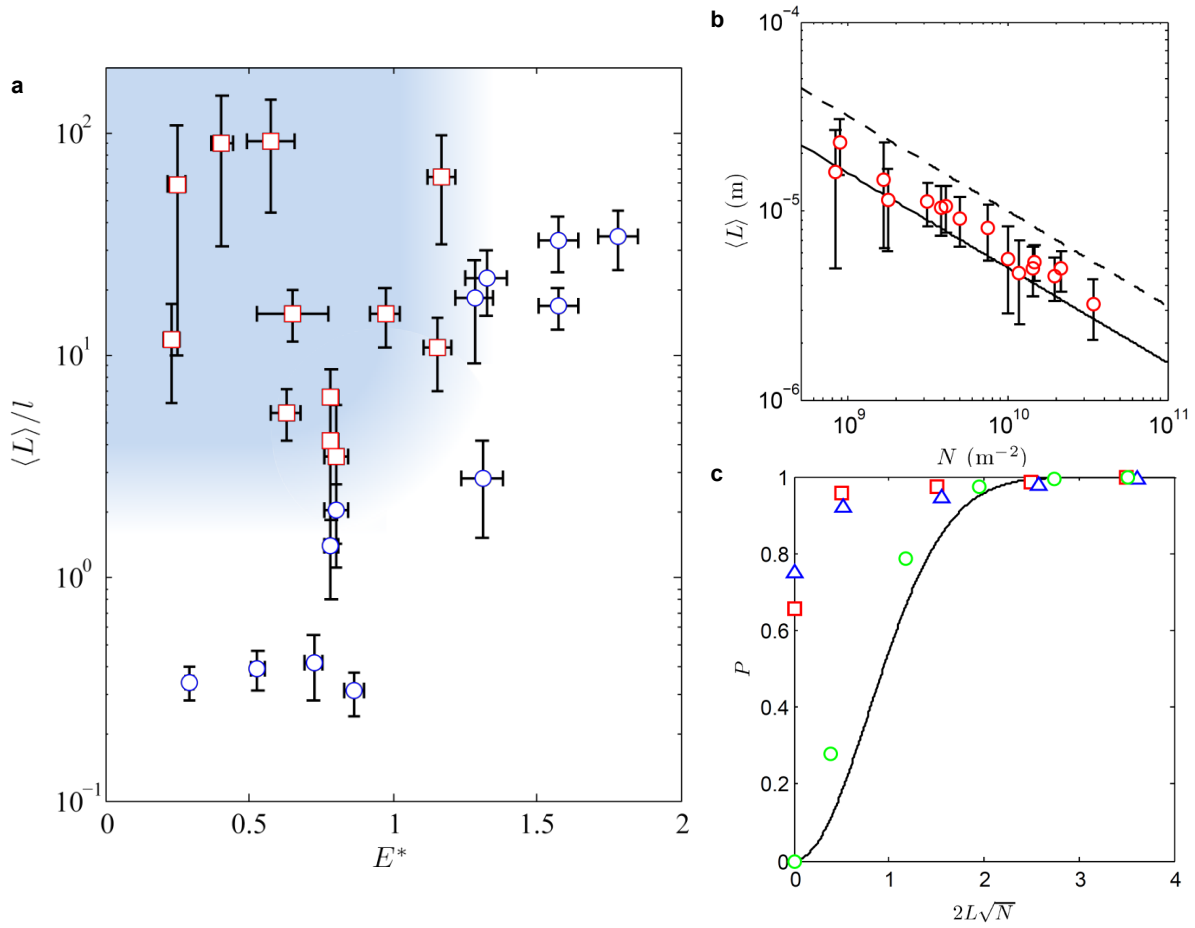

Figure 5: **Droplet morphology regime map and nucleation behaviour.** (a) Regime map characterizing the dominant wetting behavior observed during condensation with coordinates of $\langle L\rangle/l$ and E^*. Cassie morphologies (□) emerge at large $\langle L\rangle/l$ and $E^* \lesssim 1$ (shaded region). Wenzel morphologies (○) emerge at low $\langle L\rangle/l$ and/or $E^* \gtrsim 1$. The horizontal uncertainty bars were determined from the propogation of error associated with measurement of the structure geometry and θ_a. The vertical error bars represent one standard deviation in the mean seperation distance between droplets. (b) Measured mean separation distances between droplet centres for a range of samples where $\langle L\rangle/l > 1$ are shown in comparison to the Poisson distribution (solid line), which predicts a mean separation distance $L_p = (1/2)N^{-1/2}$, and for a uniform distribution (dashed line), $L_{ud} = N^{-1/2}$. Error bars represent one standard deviation. (c) Nucleation behavior on a structured silicon surface ($l = 3.5$ µm) for two different CVD silane films at a fixed location, C1 (□) & C2 (△). The nucleation sites for each coating ($n_{C1} = 247$, $n_{C2} = 263$) were repeatable as shown by the deviation of the cumulative probability distribution from the predicted Poisson behavior, $P = 1 - e^{-N\pi L^2}$. An overlay of the nucleation sites observed for C1 and C2 ($n_{C1+C2} = 151$) were found to conform closely to a Poisson distribution (○).

Supporting Information

Condensation on superhydrophobic surfaces: The role of length-scale and energy barriers

Ryan Enright[1,2], *Nenad Miljkovic*[1], *Ahmed Al-Obeidi*[1], *Carl Thompson*[1], and *Evelyn N. Wang*[1]

[1]Department of Mechanical Engineering, Massachusetts Institute of Technology, 77 Massachusetts Avenue, Cambridge, MA

[2]Stokes Institute, University of Limerick, Limerick, Ireland

S1. Supporting Movie Legends

Supporting Movie 1 Droplet growth and ejection captured using ESEM on the Si nanopillar surface shown in Figure 1e ($l = 2$ μm, $E^* = 0.63$). Coalescence-induced droplet ejection was observed towards the end of the video. Playback speed: 4x (MPEG; 28 MB). Field of view: 266 μm x 133 μm (width x height).

Supporting Movie 2 Normal zipping behavior captured using OM on a Si nanopillar surface ($l = 300$ nm, $E^* = 1.28$). Playback speed: 1/8x (MPEG; 9.1 MB). Field of view: 176 μm x 132 μm (width x height).

Supporting Movie 3 Condensation captured using OM on the Au nanopillar surface corresponding to Fig. 3a ($l = 288$ nm, $E^* = 0.61$). Playback speed: 3x (MPEG; 9.4 MB). Field of view: 176 μm x 132 μm (width x height).

Supporting Movie 4 Condensation captured using OM on the Si micropillar surface corresponding to Fig. 3c ($l = 12.5$ μm, $E^* = 0.25$). Playback speed: 10x (MPEG; 21.4 MB). Field of view: 176 μm x 132 μm (width x height).

Supporting Movie 5 Condensation captured using OM on the Si micropillar surface corresponding to Fig. 3e ($l = 4.5$ μm, $E^* = 0.71$). Playback speed: 6x (MPEG; 27.3 MB). Field of view: 176 μm x 132 μm (width x height).

Supporting Movie 6 Condensation captured using OM on the Si micropillar surface corresponding to Fig. 3g ($l = 4.5$ μm, $E^* = 0.71$). Playback speed: 3x (MPEG; 12.5 MB). Field of view: 176 μm x 132 μm (width x height).

S2. Thermodynamic Nucleation Theory

Assuming that the bulk surface tension γ and liquid density apply to the nucleus and that the vapour behaves as an ideal gas, the minimum droplet radius of curvature required for nucleation followed by stable growth can be estimated from classical nucleation theory[1] (CNT) as $R_c = 2\gamma v_o / kT_w \ln S$, where v_o is the molecular volume of the condensed phase and k is the Boltzmann constant. The supersaturation $S = p_v/p_w$ is defined as the ratio of the vapor pressure p_v to the saturation pressure p_w at the condensing surface temperature T_w. For the conditions of the ESEM experiment, $\gamma = 74.1$ mN/m and $v_o = 0.03$ nm^3, we calculate $R_c = 17.7 \pm 27.4$ nm. This size is consistent with the observation of droplet nucleation within the confines of the pillar array, $R_c \ll \sqrt{2}l - d$, and on the sides of the pillars, $R_c \ll d$.

S3. Measurement of contact angles and pinned neck size

Environmental scanning electron microscope (ESEM) images of water droplets show high topographic contrast such that reliable geometric measurements, such as contact angles, can be made[2]. Droplet contact angles, as well as the pinned neck size of the partially wetting droplet morphologies, were determined from high resolution images of the condensed droplets (see

Supporting Figure S2.1). The contact angle was calculated from the radius of the droplet and the height of the spherical segment H as

$$\theta_{app} = \sin^{-1}\left(\frac{H-R}{R}\right) + 90°. \qquad \text{Eq. S2.1}$$

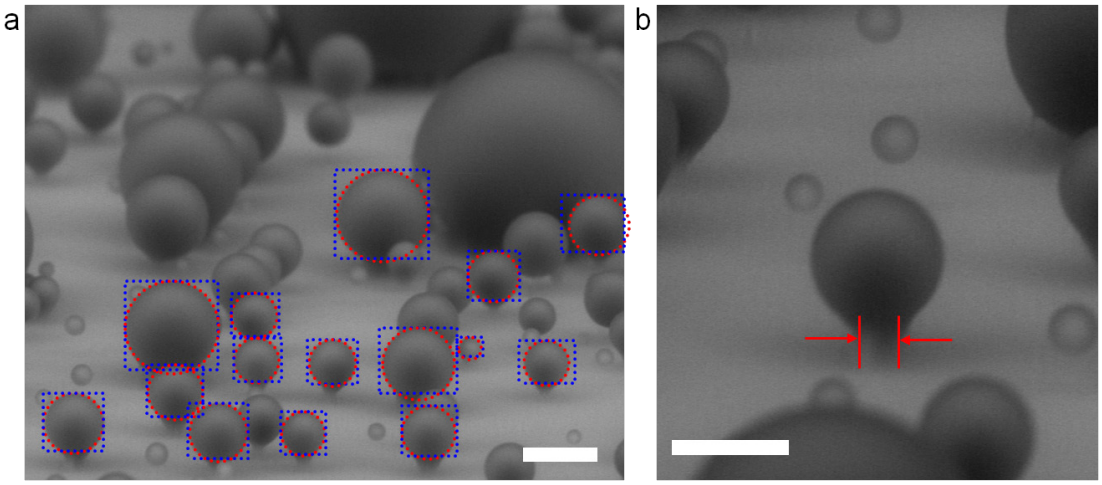

Supporting Figure S2.1 Extracting contact angles and pinned neck size from ESEM images. (a) High-resolution ESEM image of condensed droplets on the surface shown in Fig. 1a and 2a. The contact angle and diameter of the partially-pinned droplet morphologies were found by locating three points on the spherical section of the droplet. A circle passing through each of the points was then fitted giving the diameter of the droplet. A rectangular box was then fitted so that one side was tangent to the circle while the other side passed through the points where the droplet morphology deviated from the fitted circle to yield the height of the spherical segment from which the contact angle was then determined as given by Eq. S2.1. Scale bar: 30 μm. (b) Magnified view of a partially pinned droplet morphology. The pinned neck size was found by fitting two parallel lines to the base of the droplet within the structures. Scale bar: 20 μm.

S4. Estimating the energy barriers for growth beyond a single unit cell

In order to predict the initial growth route of a single droplet beyond the confines of a single unit cell, as shown in Supporting Figure S3.1a-c, an energy analysis was performed considering the geometry shown in Supporting Figure S3.1d.

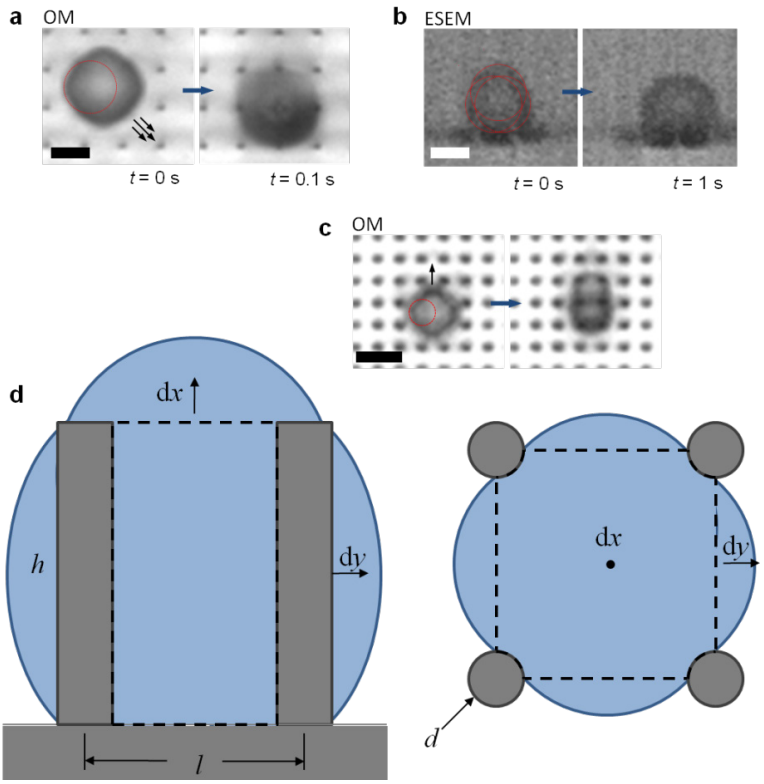

Supporting Figure S3.1 Droplet growth beyond the unit cell. Observations of a droplet growing beyond the confines of a single unit cell where (a, b) $\boldsymbol{E_u^* = 1.43}$ (l = 4 μm, r = 1.56, φ = 0.004) and (c) $\boldsymbol{E_u^* = 1.42}$ (l = 2 μm, r = 3.26, φ = 0.018). The drops demonstrate five characteristic bulges associated with the pinning barriers defined by the four sides and top of the unit cell. The likely initial growth path for the droplet is approximated by considering the magnitude of the two characteristic energy barriers located at the top of the unit cell in the x-direction and at the side of the unit cell in the y-direction shown diagrammatically in (d). Scale bars: 4 μm.

As the drop grows to occupy the volume of the unit cell it encounters two distinct energy barriers associated with the top and side of the unit cell. We approximate the magnitude of these energy barriers by considering the energy cost for an incremental increase in volume in each direction, $\mathrm{d}V_t(A_t\mathrm{d}y) \equiv \mathrm{d}V_s(A_s\mathrm{d}x)$. In the case of overcoming the energy barrier at the top of the unit cell about the pinned contact line of length πd, we find

$$\Delta E_t = \gamma_{lv}(A_t + \pi d\mathrm{d}x + 4(l-d)\mathrm{d}x) - \gamma_{lv}A_t = \gamma_{lv}\big(\pi d + 4(l-d)\big)\mathrm{d}x. \qquad \text{Eq. S3.1}$$

For the side of the unit cell we estimate the energy barrier as

$$\Delta E_s = \gamma_{lv}(A_s + 2h\mathrm{d}y + (l-d)\mathrm{d}y) + \gamma_{sl}(l-d)\mathrm{d}y - \gamma_{lv}A_s - \gamma_{sl}(l-d)\mathrm{d}y$$

$$= \gamma_{lv}\big(2h + (l-d)(1-\cos\theta_a)\big)\mathrm{d}y. \qquad \text{Eq. S3.2}$$

Comparing the ratio of the two respective energy barriers and noting the definitions for the surface roughness, $r = 1 + (\pi dh/l^2)$, and solid fraction, $\varphi = \pi d^2/4l^2$, we find

$$E_u^*(n=1) = \frac{\Delta E_t}{\Delta E_s} \qquad \text{Eq. S3.3}$$

$$= \frac{(r-1)\big(\sqrt{\pi} - 2\sqrt{\varphi}\big)\big(\pi\sqrt{\varphi} - 4\sqrt{\varphi} + 2\sqrt{\pi}\big)}{\pi(1-\varphi)\left(\sqrt{\pi}\sqrt{\varphi}(1-\cos\theta_a) + (r-1) - 2\varphi(1-\cos\theta_a)\right)},$$

where dx is related to dy by the equal volume constraint as

$$dx = \frac{1}{2}\frac{(r-1)(1-\varphi)\big(\sqrt{\pi} - 2\sqrt{\varphi}\big)}{\pi\sqrt{\varphi}}\mathrm{d}y. \qquad \text{Eq. S3.4}$$

A similar procedure can be applied to define E_u^* for a droplet occupying n unit cells prior to emergence that is given by

$$E_u^*(n) = A(n)\frac{(r-1)\big(\sqrt{\pi} - 2\sqrt{\varphi}\big)}{\pi(1-\varphi)\left(\sqrt{\pi}\sqrt{\varphi}(1-\cos\theta_a) + (r-1) - 2\varphi(1-\cos\theta_a)\right)}, \qquad \text{Eq. S3.5}$$

where the coefficient $A(n)$ is given in Supporting Table S3.1 for several values of n.

Supporting Table S3.1 Values of A as a function of the number of unit cells wetted by the droplet before emergence ($\theta_{app} > 90°$).

n	A
2	$\left(\pi\sqrt{\varphi} - 3\sqrt{\varphi} + \frac{3}{2}\sqrt{\pi}\right)$
4	$\left(\pi\sqrt{\varphi} - \frac{8}{3}\sqrt{\varphi} + \frac{4}{3}\sqrt{\pi}\right)$

6	$\left(\pi\sqrt{\varphi}-\frac{5}{2}\sqrt{\varphi}+\frac{5}{4}\sqrt{\pi}\right)$

As the droplet progressively wets units cells, E_u^* monotonically decreases as shown in Supporting Figure S3.2 for the structures shown in Fig. 2a&b. Once $E_u^* < 1$ the droplets will grow out from the structures ($\theta_{app} > 90^\circ$), entering a distinctly different growth phase that is governed by characteristic pinning barriers.

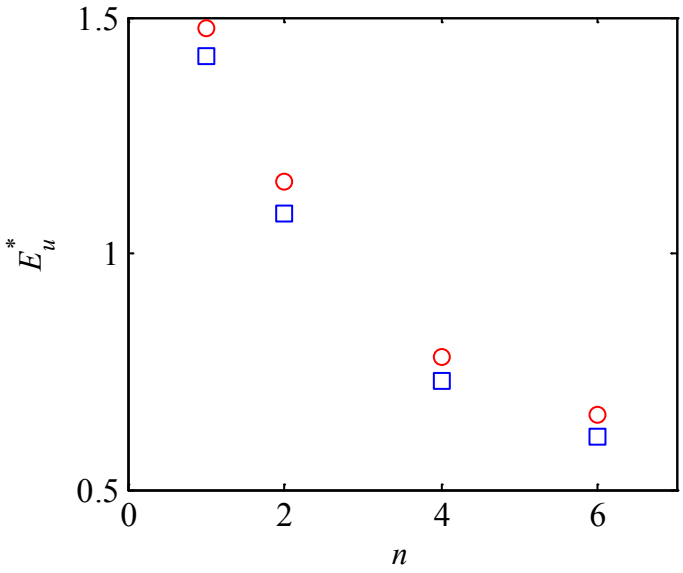

Supporting Figure S3.2 Growing out above the structures. $\boldsymbol{E_u^*}$ plotted as a function of the number of unit cells wetted by the droplet for h = 6.1 μm, d = 300 nm and l = 4 μm (□) and l = 2 μm (○). The analysis indicates that in both cases the droplet should grow out above the structures ($\boldsymbol{\theta_{app} > 90^\circ}$) when the droplet wets four unit cells.

S5. Calculating the pinning barriers

In order to calculate the pinning barriers that give rise to the observed droplet morphologies the problem was simplified to two dimensions and our attention was focused on the wetting behavior of the local contact line at individual rows of pillars as shown diagrammatically in Supporting

Figure S4.1. The angle α represents a critical angle at which the contact line can depin and wet down the side of the composite liquid-solid interface. The angle η, depicted in Supporting Figure S4.1c, represents a second characteristic pinning angle whose value depends on both the pillar geometry and the location of the pinned contact line in the preceding pillar row.

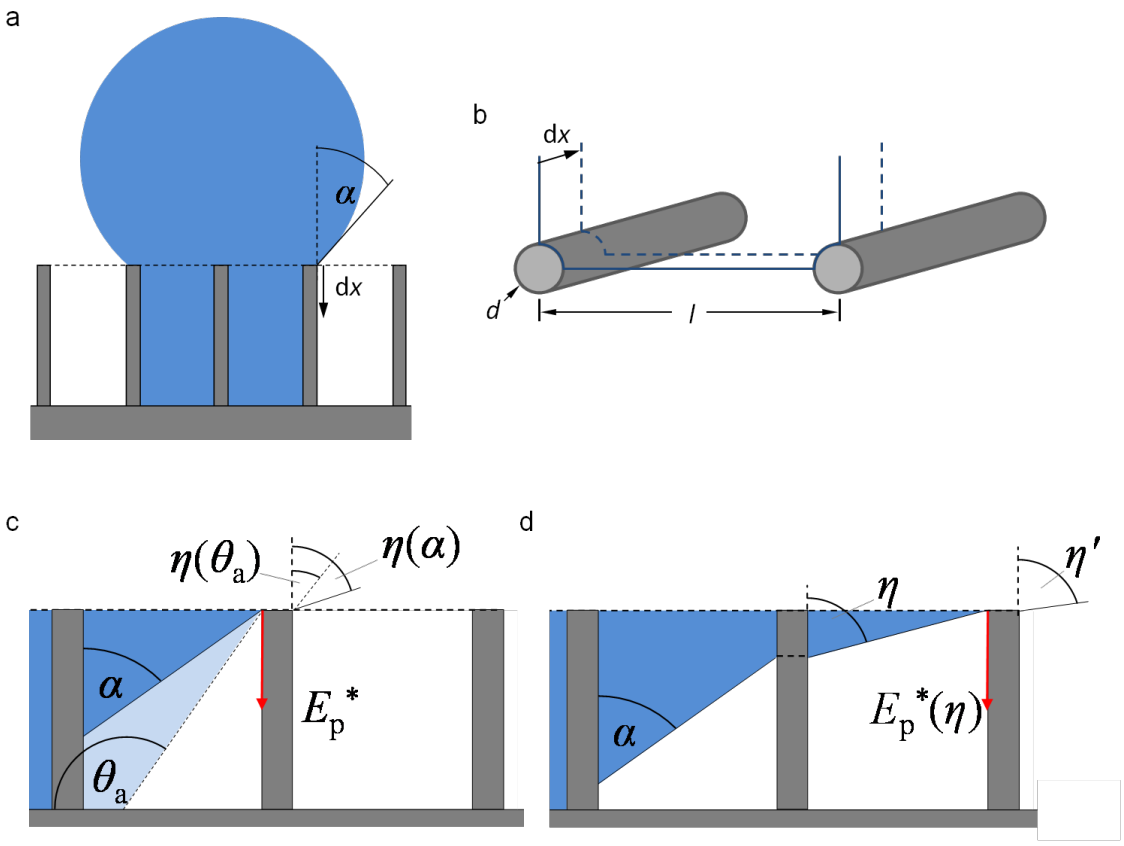

Supporting Figure S4.1 Characteristic contact line pinning angles. (a) Diagram of a droplet growing out of the structures ($\boldsymbol{E_u^* < 1}$) and reaching the first characteristic pinning barrier $\boldsymbol{\alpha}$. (b) Diagram of incremental wetting process down the sides of the pillars that defines α. The contact line translates over a composite surface composed of the pillar sides and the liquid vapor interface between the pillars. (c) Characteristic contact line pinning angle η functionally dependent on the location of the preceding pinned contact line *via* $\boldsymbol{E_p^*}$ which acts to pull the interface down. (d) Saturating behavior of the pinning angle $\boldsymbol{\eta'}$ as the interface wets subsequent rows of pillars where $\boldsymbol{E_p^*}$ is dependant on $\boldsymbol{\eta}$.

The first characteristic pinning angle, α, encountered by a droplet growing from within the pillar structures was estimated by considering the energy required for the contact line to move down

the composite liquid/solid interface comprising the outside of the wetted region of the pillars. The change in energy due to an incremental wetting of the composite surface, shown diagrammatically in Supporting Figure S4.1b, is given by

$$\Delta E = A_{sl}\gamma_{sl} - A_{sv}\gamma_{sv} - A_{lv}\gamma_{lv}, \quad \text{Eq. S4.1}$$

where γ_{sl}, γ_{sv}, and γ_{lv} are the solid/liquid, solid/vapor, and liquid vapor surface energies, respectively. The area of the solid portion wetted by the advancing contact line is given by

$$A_{sl} = A_{sv} = \frac{\pi d}{2} r_p \mathrm{d}x, \quad \text{Eq. S4.2}$$

where r_p is a local roughness factor used to account for surface roughness on the sides of the pillars and dx represents an incremental translation distance of the contact line. The area reduction of liquid/vapor interface during the wetting process is given by

$$A_{lv} = (l - d)\mathrm{d}x. \quad \text{Eq. S4.3}$$

Noting the definition of the contact angle[3], $\gamma_{lv}\cos\theta = \gamma_{sv} - \gamma_{sl}$, we find

$$\Delta E = \left[-\frac{\pi d}{2l} r_p \cos\theta - \left(1 - \frac{d}{l}\right)\right]\gamma_{lv} l \mathrm{d}x. \quad \text{Eq. S4.4}$$

The dimensionless energy is then defined[4] to give an expression for α as

$$\cos\alpha = -\frac{\Delta E}{\gamma_{lv} l \mathrm{d}x} = \frac{\pi d}{2l} r_p \cos\theta_a + \left(1 - \frac{d}{l}\right). \quad \text{Eq. S4.5}$$

Noting the definition of the solid fraction, $\varphi = \pi d^2/4l^2$, Eq. S4.5 is recast as,

$$\cos\alpha = \sqrt{\pi}\sqrt{\varphi}\, r_p \cos\theta_a + \left(1 - \frac{2\sqrt{\varphi}}{\sqrt{\pi}}\right). \quad \text{Eq. S4.6}$$

If $\alpha > \pi/2$ the situation is similar to that of a droplet wetting a hydrophobic fiber tip[5, 6] and the apparent contact angle $\theta_{app} \to \pi$ as $R \to \infty$ in the absence of interactions with other droplets and gravity. However, when $\alpha < \pi/2$ the droplet is subject to a Gibbs instability, becoming unstable when α is reached.

The second characteristic pinning angle can develop when the interface of the droplet comes into contact with the surrounding pillars without complete wetting of the intervening gap between pillar rows (see Supporting Figure S4.1c). In the limit of $R \gg l$ the angle required to depin the contact line is dependent on the energy required to wet the pillars minus a contribution from the pinned interface in the preceding row,

$$\Delta E = A_{sl}\gamma_{sl} - A_{sv}\gamma_{sv} - E_p. \quad \text{Eq. S4.7}$$

The area of the solid portion wetted by the advancing contact line is given by

$$A_{sl} = A_{sv} = \pi d r_p \mathrm{d}x. \quad \text{Eq. S4.8}$$

Making the appropriate substitutions and non-dimensionalizing the energy we find

$$\cos\eta = -\frac{\Delta E}{\gamma_{lv} l \mathrm{d}x} = 2\sqrt{\pi}\sqrt{\varphi} r_p \cos\theta_a + E_p^*. \quad \text{Eq. S4.9}$$

Thus, for the situation where the contact line remains pinned on the side of the preceding wetted pillar row the depinning angle is given by,

$$\cos\eta = 2\sqrt{\pi}\sqrt{\varphi} r_p \cos\theta_a + \cos\alpha, \quad \text{Eq. S4.10}$$

or, when the preceding is pinned at the base of the pillar structures,

$$\cos\eta = 2\sqrt{\pi}\sqrt{\varphi} r_p \cos\theta_a + \sin\theta_a. \quad \text{Eq. S4.11}$$

It then follows that the next pinning angle η' can be defined based on the value of η (see Supporting Figure S4.1d) as,

$$\cos\eta' = 2\sqrt{\pi}\sqrt{\varphi} r_p \cos\theta_a + \cos\eta. \quad \text{Eq. S4.12}$$

When *R~l*, curvature plays a significant role on the pinning behavior of the droplet by increasing the energy component acting on the contact line down. Maintaining our 2D approach we can estimate the influence of this curvature as shown in Supporting Figure S4.2. In the depicted

scenario the preceding contact line is found at the base of the pillars and is defined by the advancing angle θ_a.

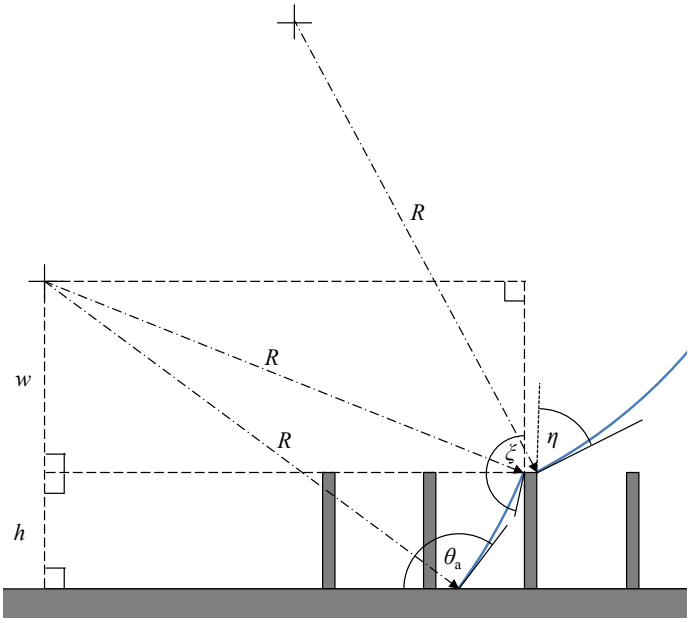

Supporting Figure S4.2 Estimating the effect of curvature on the pinning angle η. The local curvature of the interface pinned in the structures is linked to the droplet radius R to calculate the additional energy contribution to $\boldsymbol{E_p^*}$ in a simplified 2D geometry.

The vertical distance between the two contact lines is given by the height of the pillars h. The vertical distance from the top of the pillars to the centre of curvature, w, is found from

$$\sin\left(\theta_a - \frac{\pi}{2}\right) = \frac{h + w}{R}. \qquad \text{Eq. S4.13}$$

The angle that the pinned contact line makes with the row of pillars ξ can then be determined as

$$\xi = \cos^{-1}\left(\sin\left(\theta_a - \frac{\pi}{2}\right) - \frac{h}{R}\right) + \frac{\pi}{2}, \qquad \text{Eq. S4.14}$$

which, in the limit of $R \to \infty$, tends to $\xi = \theta_a - \pi/2$ as expected. We then substitute Eq. S4.14 into Eq. S4.9 and simplify to give the curvature-dependent form of the pinning angle η,

$$\cos\eta = \frac{\pi d}{l} r_p \cos\theta_a + \sqrt{1 - (\cos\theta_a + h/R)^2}. \quad \text{Eq. S4.15}$$

A similar analysis can be applied to the case where the preceding contact line wets the sides of the preceding pillar row with an angle of $\alpha + \pi/2$. The vertical distance between the two contact lines is given by the distance *x* the contact line displaces down the side of the preceding pillar row before the interface pins to the next row of pillars. This yields a similar expression to Eq. S4.15,

$$\cos\eta = \frac{\pi d}{l} r_p \cos\theta_a + \sqrt{1 - (\cos(\alpha + \pi/2) + x/R)^2}. \quad \text{Eq. S4.16}$$

Based on the local energy barriers derived above, the evolution of the droplet morphology during condensation was constructed. In Supporting Figure S4.3 the experimentally measured contact angles for the partial wetting droplet morphology on a Cassie-stable surface have been compared to the predictions of a simple 2D pinning model incorporating the characteristic angles described above.

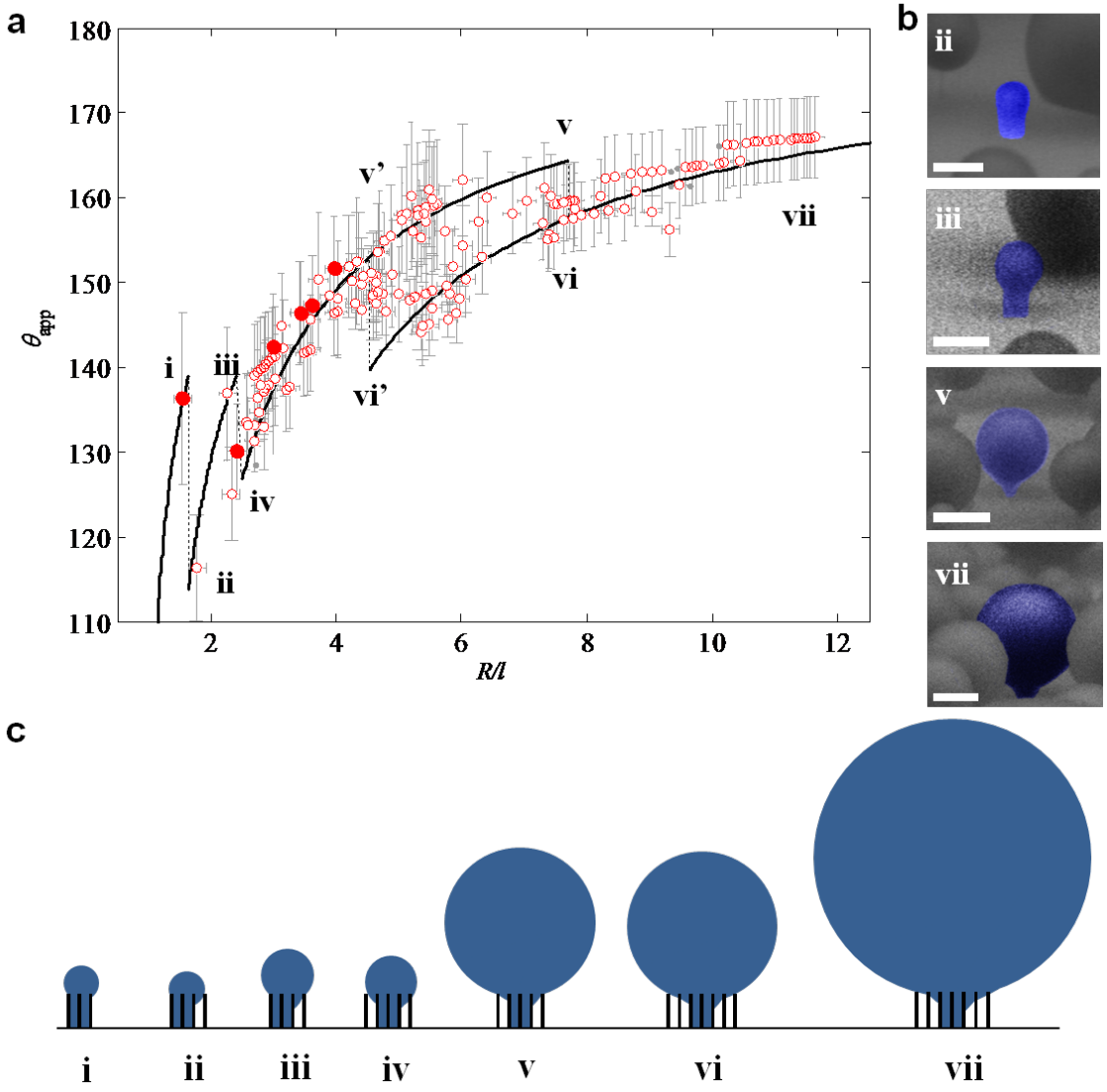

Supporting Figure S4.3 Evolution of the partially-wetting Cassie droplet morphology. Surface parameters: d = 300 nm, h = 6.1 μm, l = 2 μm, $r_p = \pi/2$ and $\boldsymbol{\theta_a = 121.6°}$ ($\boldsymbol{E^* = 0.59}$). (a) Apparent contact angle as a function of the scaled drop size. The droplet emerges from the pillar array ($\boldsymbol{\theta_{app}} > 90°$) wetting four unit cells and grows until (i) it reaches a contact angle of $\boldsymbol{\theta_{app} = \alpha + 90° \approx 139°}$ and (ii) the contact line depins resulting in sharp reduction of the apparent contact angle ($\boldsymbol{\theta_{app} \approx 114°}$) as the interface pins to the next row of pillars while maintaining constant curvature. The droplet then steadily grows to until (iii) $\boldsymbol{\theta_{app} = \alpha + 90° \approx 139°}$ and the other side of the droplet contact line depins resulting in (iv) a sharp reduction in the contact angle ($\boldsymbol{\theta_{app} \approx 123°}$) as the interface pins to the next row of pillars while maintaining constant curvature. In the absence of curvature effects on $\boldsymbol{E_p^*}$, the apparent angle then increases to (v) $\boldsymbol{\theta_{app} = \eta + 90° \approx 164°}$ before depinning, reducing to (vi) $\boldsymbol{\theta_{app} \approx 158°}$. Considering curvature effects on $\boldsymbol{E_p^*}$ with $\boldsymbol{x/R = 2/9}$, the apparent angle then increases to (v') $\boldsymbol{\theta_{app} = \eta(x/R) + 90° \approx 153°}$ before depinning, reducing to (vi') $\boldsymbol{\theta_{app} \approx 140°}$. (b) ESEM images of

the droplets at various stages of growth. Scale bars: (i, ii) 10 μm, (iii, iv) 10 μm. (c) Schematic of the evolving droplet shape predicted using the pinning model.

The droplet grows steadily up to the point where (Supporting Figure S4.3a,c(i)) $\theta_{app} = \alpha + 90° \approx 139°$ corresponding to $R = \frac{b}{2\cos\alpha} = 3.28$ μm ($R/l = 1.64$) where $b \approx 2l + d = 4.3$ μm is the width of the pinned droplet base. Once α is reached the contact line can depin and the droplet becomes unstable (see Supporting Figure S4.4). We assume that wetting occurs in an asymmetric manner with contact line advancement proceeding down one side of the wetted region due to the local energy non-uniformity of the composite contact line. The droplet is stabilized again when the interface pins to the next row of pillars. During this wetting process α must be maintained at the advancing wetting front, but conservation of mass requires constant curvature to be maintained, *i.e.*, R remains constant. This implies, as a first approximation, the formation of a non-equilibrium spindle-like morphology similar to the case of a droplet destabilizing on fiber tips where $\theta_a < 90°$ on the side of the fiber[7, 8]. We represent this geometry as a tangent line extending from the composite interface at an angle α and intercepting the spherical cap geometry. The wetting depth of the droplet at the point at which the droplet stabilizes, x, is then

$$x = \frac{R}{\sin\alpha} - \frac{1}{2}\sqrt{4R^2 - B^2} - \frac{1}{2}\frac{(2b - B)}{\tan\alpha}, \qquad \text{Eq. S4.17}$$

where $B \approx b + (l - d) = 6$ μm is the apparent base width of the stabilized droplet resulting in an estimated $x = 1.9$ μm.

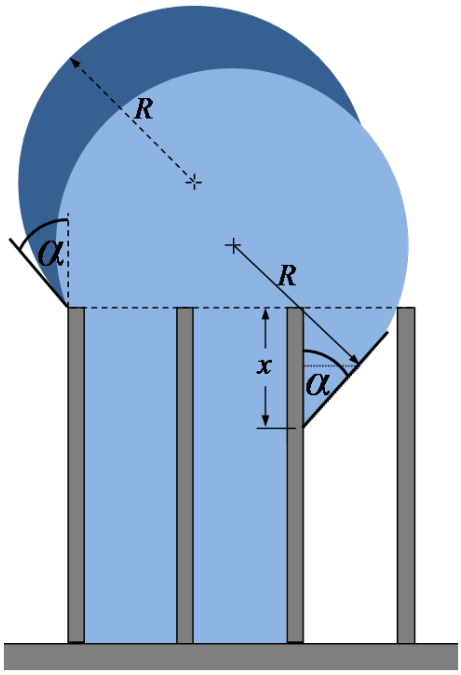

Supporting Figure S4.4 Diagram of droplet wetting after contact line depins and interface reaches the next row of pillars. To satisfy the requirement of constant curvature and mass conservation, the advancing contact line on the right side of the droplet is assumed to form a spindle-like geometry tangent to the spherical cap geometry.

The resulting droplet following this depinning event demonstrates a reduced apparent contact angle, $\theta_{app} = 114°$ (Supporting Figure S4.3a-c(ii)). The droplet radius increases further until (Supporting Figure S4.3a-c(iii)) the apparent contact angle again reaches $\theta_{app} = \alpha + 90° = 139°$ resulting in the other edge of the droplet destabilizing at constant volume resulting in a reduced apparent contact angle, $\theta_{app} = 123°$ with $R/l = 2.29$ as the interface pins on the next row of pillars (Supporting Figure S4.3a,c(iv)).

At this stage the droplet is pinned onto pillars spanning unit cells it does not completely wet and is developing the characteristic balloon neck geometry. Now de-pinning of the contact line is governed by satisfying η. We assume that the droplet contact angle and radius grows smoothly, spreading from the pinning point on the left hand side of the pillar to the right hand side of the pillar as it approaches η. We first neglect the curvature contribution so that $\theta_{app} = \eta + 90° =$

$164°$ (Supporting Figure S4.3a-c(v)). Once η is satisfied the droplet sinks uniformly with constant *R/l*, displacing the volume occupied by the vapor within the swept region. Once the interface reaches the next row of pillars on either size of the droplet the apparent angle reduces to $\theta_{app} = \eta + 90° = 158°$ (Supporting Figure S4.3a,c(vi)).

Once this stage of growth is reached the contact line remains pinned since the calculated depinning angle, $\eta' = 93° > 90°$, and the apparent contact angle tends to 180° as $R/l \to \infty$. This asymptotic behavior corresponds to the metastable Cassie state observed during the advancement of macroscopic Cassie droplets over discontinuous surface structures[9-12]. Thus, the evolution of a partially-wetting droplet on a Cassie stable surface is characterized by the interface encountering and overcoming several pinning barriers that results in an asymmetric growth processes before reaching the final pinning barrier that allows the droplet to grow into a nominally Cassie droplet.

In Supporting Figure S4.5 the experimentally measured contact angles for the partial wetting droplet morphology on a Wenzel-stable surface have been compared to the predictions of the pinning model incorporating the characteristic angles described above. In this case the curvature of the droplet relative to the spacing of the pillars plays a strong role in the emergent morphology. In developing a picture of the growth process, we again begin from a wetted state where four unit cells have been wetted during the initial phase of growth so that $E_u^* < 1$.

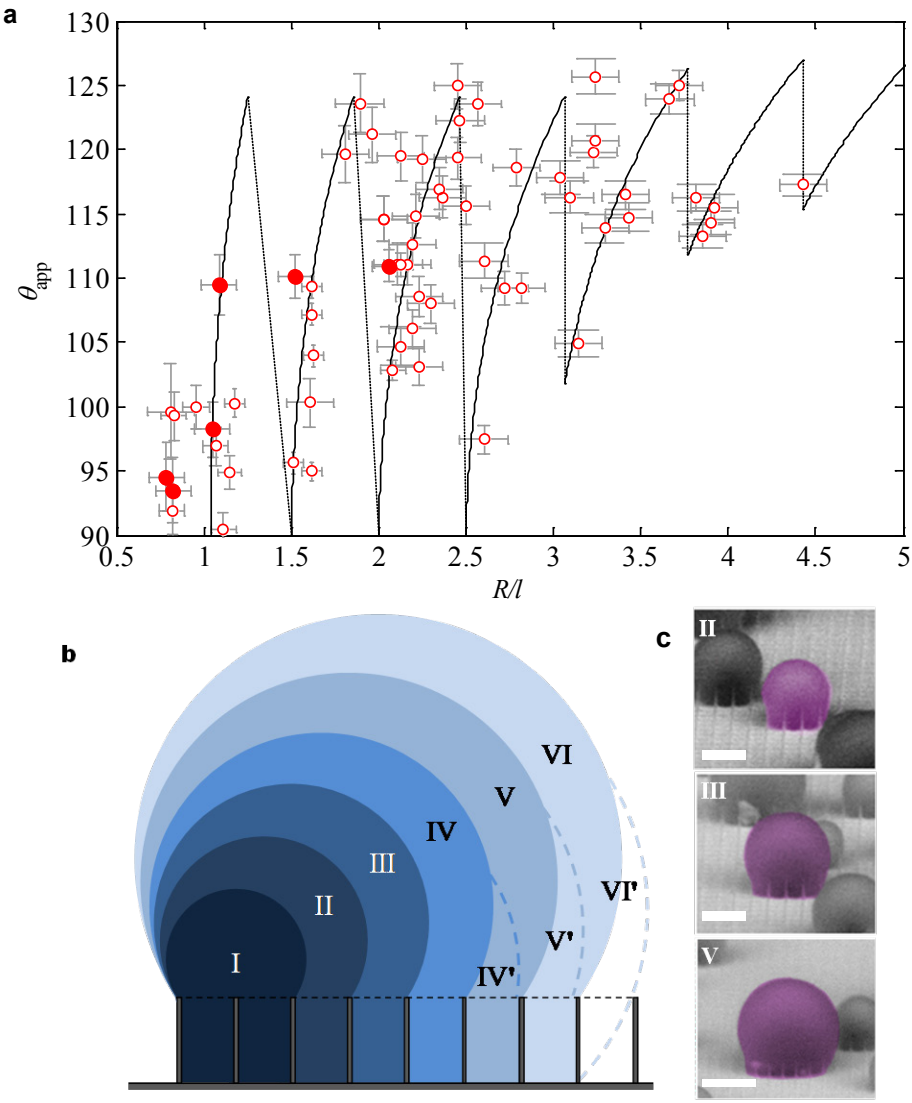

Supporting Figure S4.5 Evolution of the Wenzel droplet morphology. Surface parameters: d = 300 nm, h = 6.1 µm, l = 4 µm, $r_p = \pi/2$ and $\boldsymbol{\theta_a = 121.6°}$ ($\boldsymbol{E^* = 1.22}$). (a) Measured apparent contact angle as a function of the scaled drop size compared to the simple 2D pinning model. (b) Diagram of the evolving droplet shape predicted by the simple 2D pinning model. The dashed lines correspond to the droplet pinning to the next row of pillars with an apparent contact angle $> 90°$. (c) Selection of condensed droplets captured using ESEM approaching the limits of the pinning barrier ($\boldsymbol{\theta_{app} \approx 125°}$). Scale bar: (II, III) 10 µm, (V) 15 µm.

The droplet grows steadily up to the point where (Supporting Figure S4.5a,c(I)) $\theta_{app} = \alpha + 90° \approx 124°$ corresponding to $R = \frac{b}{2\cos\alpha} = 5$ µm, where $b \approx 2l + d = 8.3$ µm is the width of the pinned droplet base. Once α is reached, the contact line can de-pin and the droplet becomes

unstable. The wetting proceeds in an asymmetric manner with the contact line advancing down one side of the wetted region due to the composite, non-homogenous nature of the droplet base perimeter. This asymmetric wetting process was captured using OM (Supporting Figure S4.6). Typically, depinning was found to occur at one edge the wetted region resulting in the periodic translation of the droplet centre of mass. In contrast to the growth of a partially wetting droplet, the periodic depinning events led to wetting at the base of the pillars resulting in the propagation of complete wetting under the droplet.

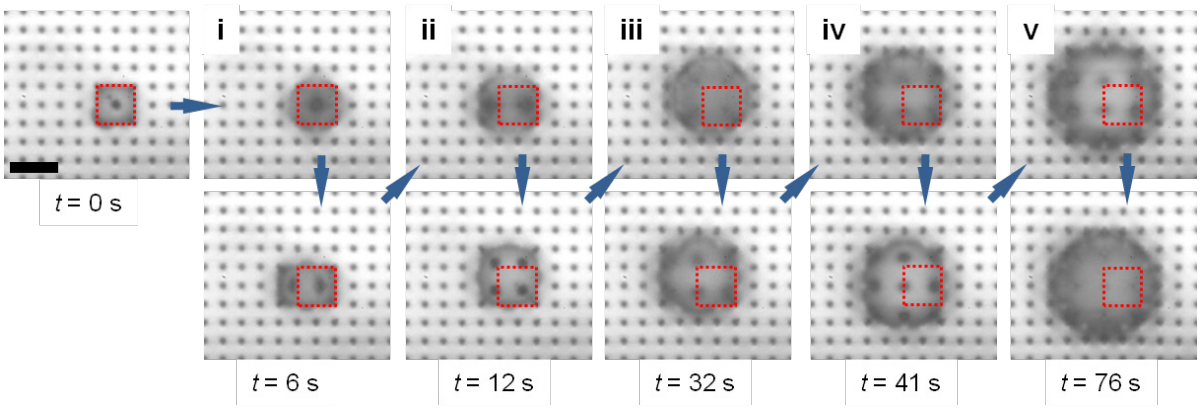

Supporting Figure S4.6 Evolution of the Wenzel droplet morphology observed using OM. (a) The droplet emerges from the pillar array ($\boldsymbol{\theta_{app}} > 90°$) wetting four unit cells and grows until (i) it reaches a critical apparent contact angle ($\boldsymbol{\theta_{app}} = \boldsymbol{\alpha} + \mathbf{90°} \approx \mathbf{124°}$) before the contact line depins resulting in the droplet wetting two neighboring unit cells. (ii) The droplet continues to grow wetting an area of 3 x 2 unit cells. The smaller of the two radii of curvature dictates the direction of the next depinning event resulting in the droplet wetting three neighboring unit cells, thus tending to a more symmetric droplet shape spanning 3 x 3 unit cells. From (iii) to (iv) the droplet undergoes a similar wetting process as (i) to (ii). Several depinning events later and the wetted base of the droplet began to develop an octagonal shape with the contact line spanning diagonals of unit cells at the 'corners' of the droplet. The red box outlines the original four unit cells where the droplet originated from highlighting the movement of the droplet centre of mass during growth as a result of the asymmetric wetting process. Scale bar: 5 μm.

S6. Optical microscopy experimental set-up

Droplet growth behavior was studied using a custom set-up shown diagrammatically in Supporting Figure S5.1. A supply of water-saturated N_2 was obtained by sparging a temperature-controlled water reservoir with dry N_2. A reservoir by-pass valve was installed to provide dry N_2

to the sample as it was being cooled to the test temperature at the beginning of each experiment. The sample temperature was set using a temperature-controlled stage (Instec, TS102-00). Good thermal contact between the sample and the temperature control stage was obtained by interposing a thin layer of thermal grease (Omegatherm, Omega) with a thermal conductivity of 2.2 W/m.K. Once the stage temperature stabilized to the test temperature, typically T_w = 283 K, the by-pass valve was closed to initiate the flow of water-saturated N_2 to the sample enclosure at a constant flow rate of Q = 2.5 L/min, marking the start of the experiment. The chamber humidity (Hygroclip, Rotronic) was recorded throughout the experiment. The supersaturation was controlled by adjusting the water reservoir temperature through which the N_2 was sparged. Droplet nucleation and growth was recorded at intervals of 0.1 seconds using a CMOS camera (Phantom v7.1, Vision Research), operating at a resolution of 800 x 600 and a physical pixel size of 22 μm, attached to an upright microscope (Eclipse LV100, Nikon). Imaging was performed with either a 40x (Plan Fluor ELWD, Nikon) or a 100x (L Plan SLWD, Nikon) objective. The relationship between length and pixel count was calibrated with the known pillar spacing of a microstructured surface previously found using SEM.

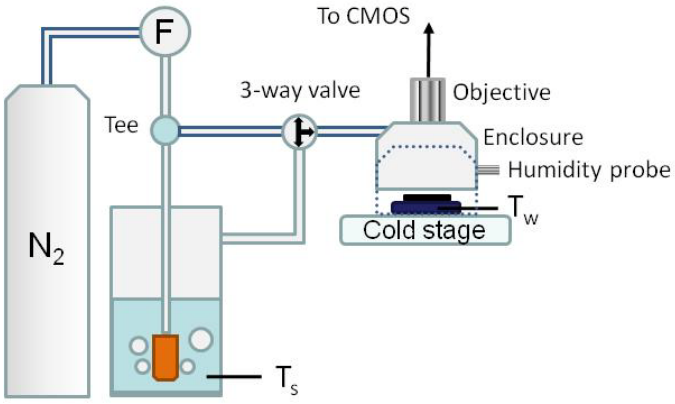

Supporting Figure S5.1 Optical microscopy experimental set-up. The mounted sample was first cooled to the test temperature by the temperature-control stage under an atmosphere of dry N_2. Following thermal equilibration, a three-way valve was actuated to route the N_2 supply

through a temperature-controlled water reservoir *via* a sparging head. The chamber humidity was measured using a humidity probe located ~1 cm from the mounted sample. The process of initial droplet nucleation and growth was captured at either 40x or 100x magnification using a CMOS camera mounted to an upright microscope.

S7. Observation of Cassie and Wenzel wetting regions using OM

The wetting behavior observed using OM is shown in Supporting Figure S6.1 where we tracked the coalescence of two droplets growing in the Wenzel state beyond the transition point ($E^* > 1$) as evidenced by the dark square-shaped regions under the droplets at $t = 0$ s. Upon coalescence a light reflecting region was apparent under the newly-formed droplet indicating the presence of a liquid/vapour interface. The wetting transition after coalescence was slow and over the course of the next 40 s the wetting front advanced in a geometrically-ordered fashion from the originally pinned areas until the base of the droplet was in the Wenzel state.

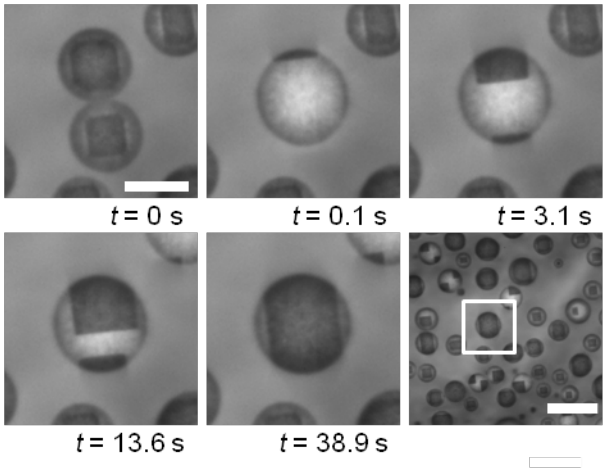

Supporting Figure S6.1 Identification of Cassie and Wenzel wetting states using OM. Time-lapse images show the progression of Wenzel wetting after the coalescence of two droplets for $\boldsymbol{E^* = 1.28 \pm 0.06}$ corresponding to the surface shown in Fig. 3a(ii). The contact area under the droplet(s) was observed by focusing through the droplet(s) to show the wetting state. The darker regions correspond to Wenzel wetting; the lighter to Cassie wetting. Scale bar: 10 μm. The last frame shows a zoomed out view of the surface at t = 38.9 s. Scale bar: 30 μm.

S8. Non-zipping regime in the presence of defects

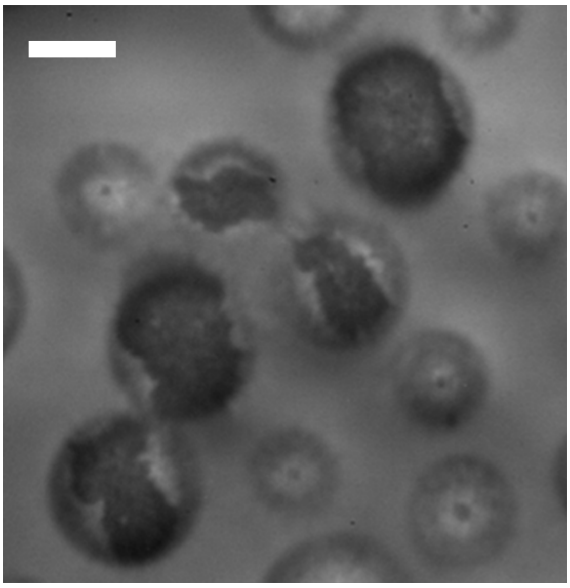

Supporting Figure S7 Non-zipping regime. Wetted defect regions revealed underneath droplets on the surface shown in Fig. 3a(i). For this geometry and intrinsic advancing wetting angle, zipping is suppressed allowing for the irregular wetting patterns to persist as the droplets grew in size, *i.e.*, wetting did not propagate on the surface. Scale bar: 10 μm.

S9. Zipping barrier

An expression for the zipping energy barrier was derived to incorporate the physical picture shown in Supporting Figure S8.1 and to explain the data presented in Fig. 3c that could not be captured by the existing criterion developed by Sbragaglia *et al.* for arrays of square pillars[13] since a unique value cannot be specified for the gap spacing between circular pillars.

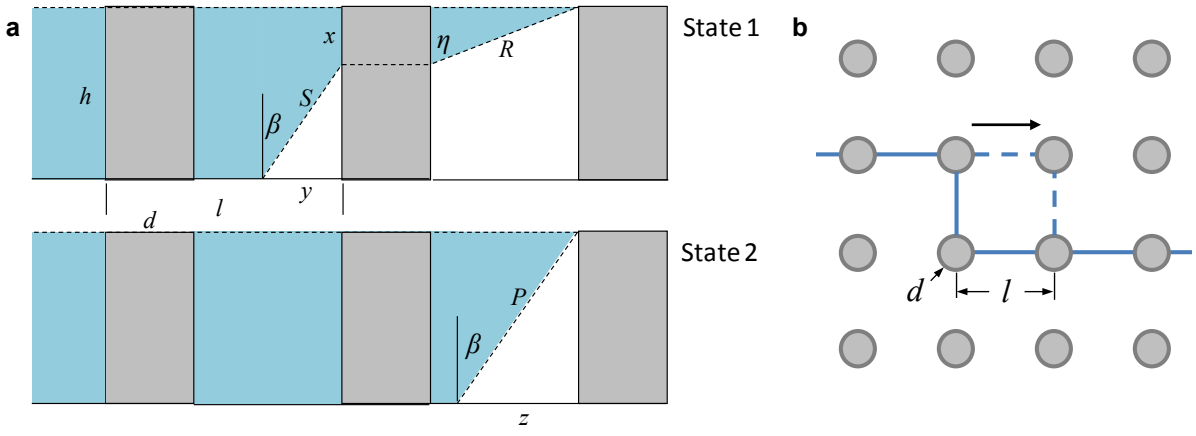

Supporting Figure S8.1 Normal zipping barrier schematic. (a) The energy required for zipping wetting perpendicular to the normal wetting front is determined by considering the energy difference between the limiting pinned state (State 1) and an intermediate pinned state following wetting of the unit cell (State 2). (b) Schematic top view of the normal zipping process. The arrow shows the direction of wetting from State 1 to State 2. The solid line marks the middle pillar in State 1 shown in (a).

The interface is initially pinned and spans two unit cells in the axial direction (Supporting Figure S8.1, State 1). Wetting proceeds from above[14] and propagates along the axis of the pillar array perpendicular to the advancing wetting front (zipping) resulting in the contact line displacing to an intermediate pinned position (Supporting Figure S8.1, State 2). Following the zipping process the interface returns to the shape shown in State 1, but shifted one row forward. The energy change from State 1 to State 2 is found from

$$\Delta E_{zip} = \gamma_{sl}\left(A_{sl,2} - A_{sl,1}\right) + \gamma_{sv}\left(A_{sv,2} - A_{sv,1}\right) + \gamma_{lv}\left(A_{lv,2} - A_{lv,1}\right), \quad \text{Eq. S8.1}$$

where

$$A_{sl,1} = \pi d(h + x) + l(l - y) + \frac{1}{4}\pi d^2, \quad \text{Eq. S8.2}$$

$$A_{sv,1} = ly + \pi d(h - x) + l^2 - \frac{1}{4}\pi d^2, \quad \text{Eq. S8.3}$$

$$A_{lv,1} = l(S + R + d) - \frac{1}{4}\pi d^2, \quad \text{Eq. S8.4}$$

$$A_{sl,2} = 2\pi dh + l^2 + l(l - z), \quad \text{Eq. S8.5}$$

$$A_{sv,2} = zl, \quad \text{Eq. S8.6}$$

$$A_{lv,1} = Pl, \quad \text{Eq. S8.7}$$

and

$$x = \frac{l - d}{\tan\eta}, \quad \text{Eq. S8.8}$$

$$R = \frac{l-d}{\sin\eta}, \qquad \text{Eq. S8.9}$$

$$S = \frac{h-x}{\cos\beta}, \qquad \text{Eq. S8.10}$$

$$y = (h-x)\tan\beta, \qquad \text{Eq. S8.11}$$

$$z = h\tan\beta, \qquad \text{Eq.S8.12}$$

$$P = \frac{h}{\cos\beta}, \qquad \text{Eq. S8.13}$$

with η given by Eq. S4.11. Noting the definitions of r and φ, Eq. S8.1 can then be recast in dimensionless form as

$$\begin{aligned}\Delta E^*_{zip,n} &= \frac{\Delta E_{zip,n}}{\gamma_{lv} l^2} \\ &= -\frac{1}{\sqrt{\pi}\sin\theta_a \sin\eta}\Big[([(4\varphi\cos\eta + (r-\varphi)\sin\eta)\cos\theta_a + 1 \\ &\quad - \varphi\sin\eta]\sin\theta_a - \cos\eta + \cos^2\theta_a\cos\eta)\sqrt{\pi} \\ &\quad - 2\sqrt{\varphi}\big((1-\sin\eta+\pi\cos\theta_a\cos\eta)\sin\theta_a - \cos\eta \\ &\quad + \cos^2\theta_a\cos\eta\big)\Big]. \qquad \text{Eq. S8.14}\end{aligned}$$

When $\Delta E^*_{zip,n} < 0$, wetting leads to a reduction in energy such that zipping is spontaneous.

The physical picture of the zipping process developed here was validated by re-deriving Eq. S8.14 for a square pillar geometry and making comparison to the prediction given by Sbragaglia *et al.*[13] in dimensionless form,

$$\frac{\Delta E_s}{\gamma_{lv} l \mathrm{d}x} = -\left[\left(1-\frac{d}{l}\right) + \left(\frac{2h}{l} + 1 - \frac{d}{l}\right)\cos\theta\right]. \qquad \text{Eq. 8.15}$$

The result of the comparison is shown in Supporting Figure S8.2 and demonstrates the ability of the above analysis to capture the zipping transition point observed both experimentally and numerically by Sbragaglia *et al.*

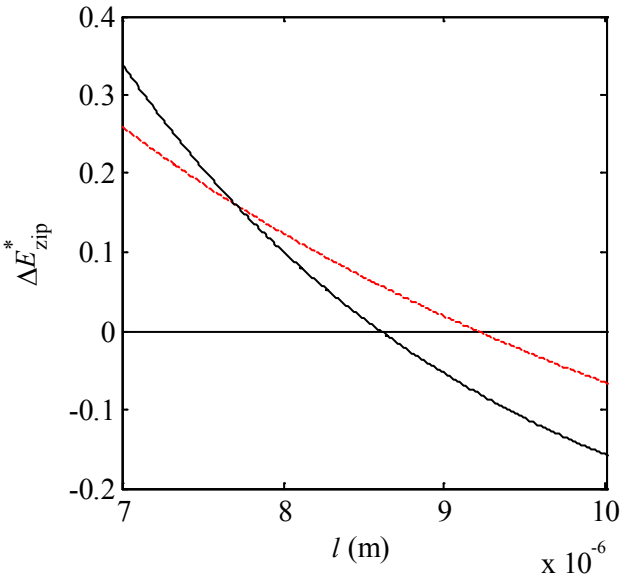

Supporting Figure S8.2 Validating the zipping expression. The zipping criterion derived by Sbragaglia *et al.* (Eq. S8.15, dashed line) compared to the expression derived here given by Eq. S8.14 (solid line). The limits of the *abscissa* (l = 7 μm and l = 1 0 μm) correspond to the geometries observed by Sbragaglia *et al.*, both experimentally and numerically, to delineate the zipping regime.

The diagonal zipping barrier can be calculated by considering the geometry shown in Supporting Figure S8.3.

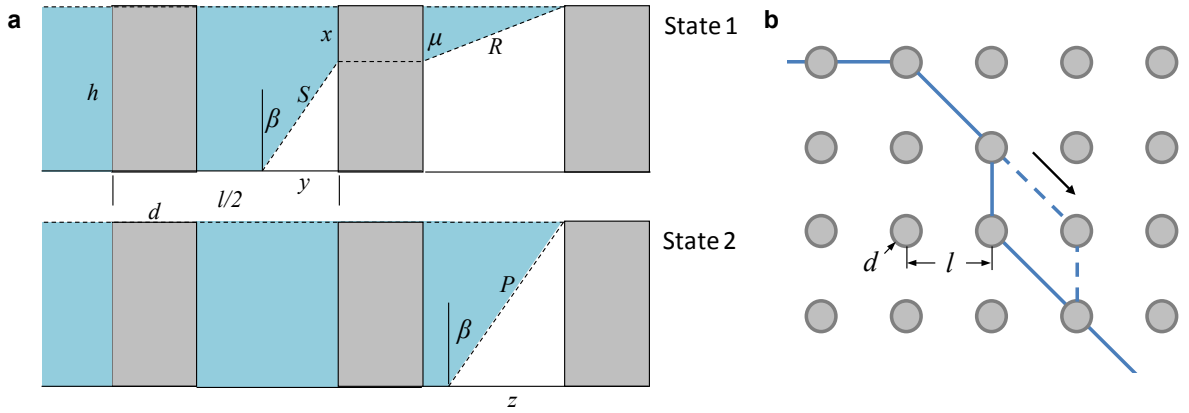

Supporting Figure S8.3 Diagonal zipping barrier schematic. (a) The energy required for zipping wetting perpendicular to the diagonal wetting front is determined by considering the

energy difference between the limiting pinned state (State 1) and an intermediate pinned state following wetting of the unit cell (State 2). (b) Schematic top view of the diagonal zipping process. The arrow shows the direction of wetting from State 1 to State 2. The solid line marks the middle pillar in State 1 shown in (a).

Following a similar calculation procedure as detailed above for the normal

zipping barrier we find

$$\Delta E^*_{zip,d} = \frac{\Delta E_{zip,d}}{\gamma_{lv} l^2}$$

$$= -\frac{1}{\sqrt{\pi}\sin\theta_a \sin\mu}\Big[\big([(4\varphi\cos\mu + (r-\varphi)\sin\mu)\cos\theta_a + 1$$

$$-\varphi\sin\mu]\sin\theta_a - \cos\mu + \cos^2\theta_a\cos\mu\big)\sqrt{\pi}$$

$$-\sqrt{2}\sqrt{\varphi}\big((2 - 2\sin\mu + \pi\cos\theta_a\cos\mu)\sin\theta_a - 2\cos\mu$$

$$+ 2\cos^2\theta_a\cos\mu\big)\Big], \qquad \text{Eq. S8.16}$$

where the angle μ is the diagonal analog to the angle η given by

$$\cos\mu = -\frac{\Delta E}{\gamma_{lv}\sqrt{2}l\mathrm{d}x} = \sqrt{2}\sqrt{\pi}\sqrt{\varphi}r_p\cos\theta_a + \sin\theta_a. \qquad \text{Eq. S8.17}$$

In Supporting Figure S8.4 the calculated dimensionless zipping energies are plotted for the geometries and intrinsic advancing contact angles corresponding to Figure 3c. The zipping barriers demonstrate a characteristic behavior of $\Delta E^*_{zip,d} - \Delta E^*_{zip,n} = const.$ for a given φ and θ_a and a small window, in terms of h, where one zipping mode is favored while the other is suppressed, $\Delta h \lesssim 10$ nm.

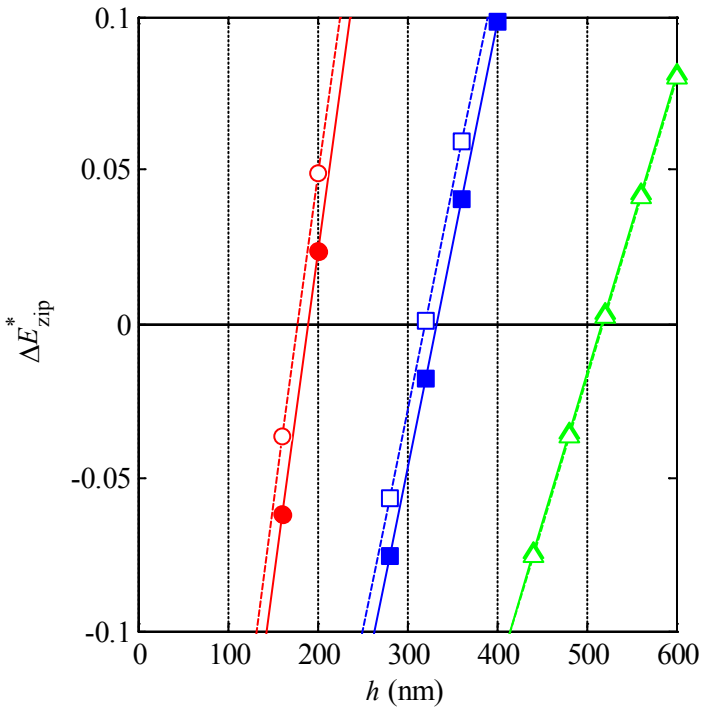

Supporting Figure S8.4 Zipping barriers. Dimensionless normal (Eq. S8.14, solid symbols) and diagonal (Eq. S8.16, open symbols) zipping energies as a function of pillar height for (○) $\theta_a = 121.6°$, (□) $\theta_a = 110.8°$ and (△) $\theta_a = 103.8°$ where $d = 108$ nm and $l = 288$ nm.

S10. Droplet growth behavior on the Au nanopillars

The global growth behavior of droplets on the Au nanopillars corresponding to Supporting Movie 3 is shown in Supporting Figure S9.1. The onset of droplet coalescence began at $t \approx 7$ s. Between t = 30 s and t = 42 s we observe a sudden slope change in the droplet number density, which coincided with the visual observation of droplet ejections resulting in the removal of droplets from the field of view. For $t > 90$ s, the average droplet size and density averaged over several minutes was approximately constant at $\langle R \rangle = 5.8 \pm 3.9$ μm and $\langle N \rangle = 2.2x10^9 \pm 5x10^8$ m^{-2}, respectively, indicating a balance between droplet shedding and re-growth was achieved.

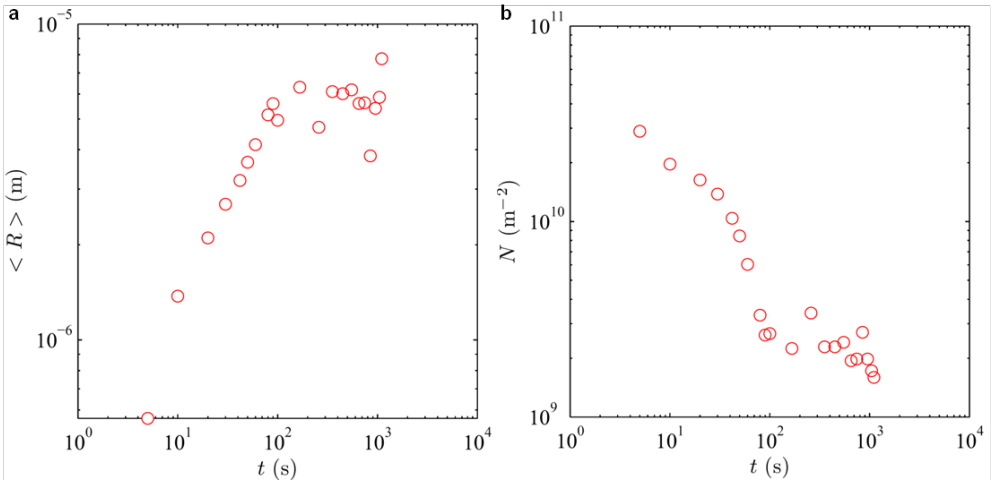

Supporting Figure S9.1 Evolution of the (a) average droplet radius and (b) droplet density on the Au nanopillar surface observed using OM as shown in Video 3. Nucleation conditions: $T_w = 283 \pm 0.1$ K, $S_{max} = 1.6 \pm 0.05$.

S11. Coalescence-induced wetting transitions

The wetting transition induced by the coalescence of two partially wetting droplets separated by a distance > l as observed in Fig. 3g,h can be understood by considering the coalescing droplet geometry shown in Supporting Figure S10.1a, where the two droplets are separated by a single unwetted unit cell. When the two drops coalesce complete wetting will be induced provided that $\alpha < 90°$ since the contact line cannot pin as the interface reconfigures to a (meta)stable state. If the droplets are now separated by a distance of 3l with two unwetted unit cells separating them, as shown in Supporting Figure S10.1b, then the transition must result in the local reduction of free energy,

$$\Delta E = A_{sl}\gamma_{sl} - A_{sv}\gamma_{sv} - 2E_p^* < 0. \qquad \text{Eq. S10.1}$$

Neglecting curvature effects, E_p^* can be estimated as $\cos\alpha$ to give,

$$\Delta E = \left[-\frac{\pi d}{l} r_p \cos\theta_a - 2\cos\alpha\right]\gamma_{lv} l dx < 0. \qquad \text{Eq. S10.2}$$

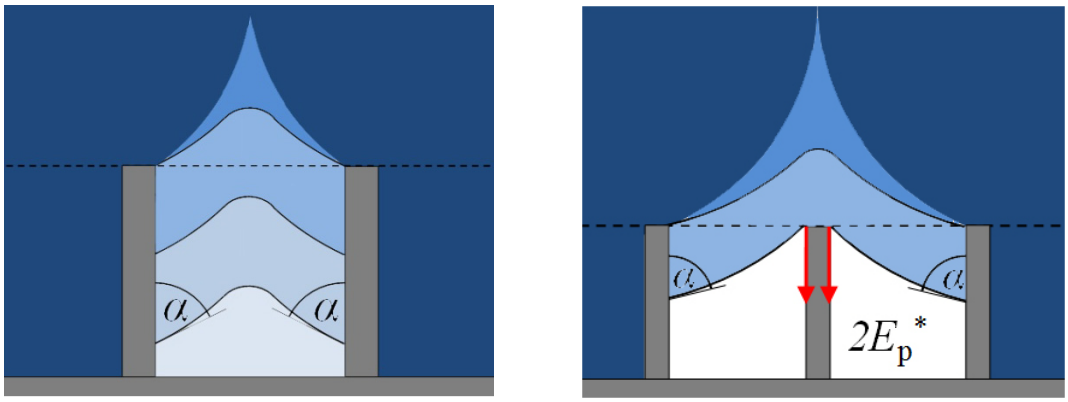

(a) (b)

Supporting Figure S10.1 Multiple droplet wetting interactions. (a) Coalescence-induced wetting transition for two droplets separated by a single, unwetted unit cell where $\alpha < 90°$. (b) Complete wetting prevented as the contact line pins on the row of pillars separating two droplets spaced 3l apart, $\Delta E/(\gamma_{lv} l \mathrm{d}x) > 0$.

S12. Nucleation Behavior

To explore the nucleation phenomenon on these hydrophobic surfaces, a series of companion experiments were performed using OM to detail the density and distribution of nucleated droplets on a range of surface geometries. The distribution of nucleation sites were found to follow Poisson statistics suggesting a spatially random process (see Figure 5b). While this result appears consistent with the stochastic nature of the nucleation process, the observed critical supersaturation is in disagreement with classic nucleation theory (CNT).

The nucleation rate (J); which is highly sensitive to the supersaturation (S) and the equilibrium wetting angle (θ_e), was calculated using CNT[1]. The dimensionless energy barrier is given by $G^* = 16\pi\psi v_o^2\gamma^3/3(kT)^2\,(\ln S)^2$, where ψ is the activity factor that accounts for the contact angle. The stationary nucleation rate for progressive nucleation is given by

$$J = zf^* \exp(-G^*), \qquad \text{Eq. S11.1}$$

where the Zeldovich factor is given by

$$z = (kT \ln S)^2 / 8\pi v_o \sqrt{kT\psi\gamma^3} \qquad \text{Eq. S11.2}$$

and f^* is the frequency of monomer attachment to the critical droplet nucleus. The monomer attachment frequency is dependent on the nature of the nucleus growth. The main modes of growth during initial heterogeneous nuclei condensation are limited to surface diffusion or direct impingement of monomer to the nucleus[15, 16]. Additionally, volumetric diffusion is a third mode of growth but is only considered important in nucleation in liquid or solid solutions[1]. In order to compare the three growth mechanisms, nucleation rates were calculated for all three.

The frequency of monomer attachment due to direct impingement is given by

$$f^*_i = \gamma_n[(1 - \cos(\theta_w))/2\psi^{2/3}](36\pi v_o^2)^{1/3} I n^{2/3}, \qquad \text{Eq. S11.3}$$

where γ_n is the sticking coefficient ($0 < \gamma_n < 1$), $I = P/\sqrt{2\pi m_o kT}$ is the classical Hertz-Knudsen impingement rate, n is the number of molecules in the nucleated cluster, v_o is the volume of a water molecule ($v_o = 3 \times 10^{-29}$ m^3). To determine an upper bound on the nucleation rate, a sticking coefficient of one is assumed ($\gamma_n = 1$).

The frequency of monomer attachment due to surface diffusion is given by

$$f^*_{sd} = \gamma_n c^* {\lambda_s}^2 I \qquad \text{Eq. S11.4}$$

where c^* is the capture number due to surface diffusion ($1 < c^* < 5$), and λ_s is the mean surface diffusion distance of an adsorbed monomer on the substrate. The capture number c^* is size independent and approximately equal to 1.9 for heterogeneous condensation of water vapor[17]. The mean surface diffusion distance is dependent on the wettability of the substrate and is given by

$$\lambda_s = \sqrt{D_{sd}\tau_d}, \qquad \text{Eq. S11.5}$$

where $D_{sd} = {d_s}^2 \nu_s \exp[-E_{sd}/kT]$ is the surface diffusion coefficient, $\tau_d = (1/\nu_s)\exp[-E_{des}/kT]$ is the desorption time, $\nu_s = V_D a/2$ is the Debye approximation of the adsorbed molecule vibration frequency, d_s is the length of a molecular jump along the substrate surface approximated by the lattice constant of the substrate ($d_s = a$ = 5.4 Å)[18] and V_D is the speed of sound in the substrate (V_D = 8433 m/s). The desorption and surface diffusion energies are given by $E_{des} = E_1 + \sigma_{sv} a_o$ and $E_{sd} = 0.5E_{des}$[19], respectively, where E_1 is the binding energy of an n = 1 sized cluster (E_1 = 0), σ_{sv} is the solid vapor interfacial energy and a_o is the water molecule surface area (a_o = 4.67 x 10^{-19} m^2). The calculated energies of desorption show excellent agreement with that of experiment and molecular dynamics simulations ($E_{des,\ SiO2}$ = 0.9 eV)[20, 21].

The frequency of monomer attachment due to volumetric diffusion is given by

$$f^*_{vd} = \gamma_n(1 - \cos\theta_w/\psi^{1/3})(6\pi^2 v_o)^{1/3} DCn^{1/3}, \qquad \text{Eq. S11.6}$$

where $D = (3/8\pi n_o {d_o}^2)\sqrt{kT/\pi m_o}$ is the self diffusion coefficient of water vapor; $C = (1/a_o)\exp(-W_1/kT)$ is the equilibrium concentration of monomers, d_o, m_o and n_o are the water molecule diameter (d_o = 3.0 Å), mass (m_o = 3 x 10^{-26} kg), and number density ($n_o = N_a/(v_o M)$), respectively[1].

The calculated critical supersaturation values (S_c) required for nucleation on the functionalized surfaces in this study ($\theta_w \approx 110°$) at T = 10 °C are 3.21 and 3.27 and 5.26 for surface diffusion, impingement and volumetric diffusion limited growth, respectively. However, the experimentally measured critical supersaturation was much lower (S_c ~ 1.0 – 1.1) (see Supporting Figure S11.1). Note that the critical supersaturation required for nucleation on clean silica ($\theta_w \leq 10°$) is $S_c \leq 1.01$, *i.e.*, adsorption limit.

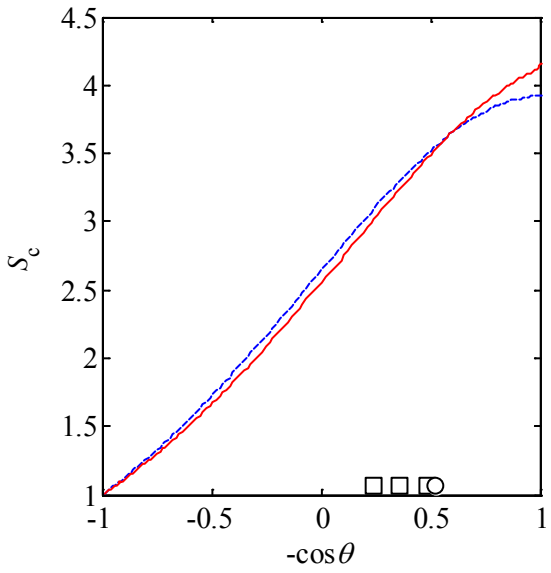

Supporting Figure S11.1 Nucleation kinetics. Predicted critical supersaturation as a function of equilibrium contact angle. The solid line corresponds to nucleation controlled by surface diffusion, the dashed line corresponds to nucleation controlled by direct impingement. The critical supersaturation observed for the silane (□) and thiol (○) coatings during ESEM and OM measurements as a function of the macroscopically measured advancing contact angles were found to occur at $S \approx 1$.

To explain this phenomenon, a structured Si surface was silanated and nucleation experiments were performed three times at the same location using OM. Subsequently, the silane film was removed with oxygen plasma, the sample was recoated, and the nucleation experiment was again repeated at the same location four times. For all experiments the supersaturation never exceeded $S = 1.4$. The spatial distribution of the nucleation sites (see Supporting Figure S11.2a,b) were compared to the cumulative Poisson probability $P = 1 - e^{-N\pi L^2}$ in Figure 5c. We found that the nucleation locations on both coatings, C1 and C2, demonstrated a high level of repeatability between consecutive runs inconsistent with temporally random behavior. However, a superposition of the nucleation locations found on C1 and C2 was found to be in good agreement with the predicted distribution suggesting that the two populations were unrelated, indicating that the observed nucleation was occurring on the underlying silicon substrate due to randomly distributed surface defects on the functional coating. The minimum size of these

defects was estimated by considering the energy barrier overcome by the growing droplet in order to spread over the hydrophobic film as $R_{d,min} \sim R_c \approx 15$ nm, which is consistent with previous measurements of vacancy defect sizes in self-assembled molecular films[22].

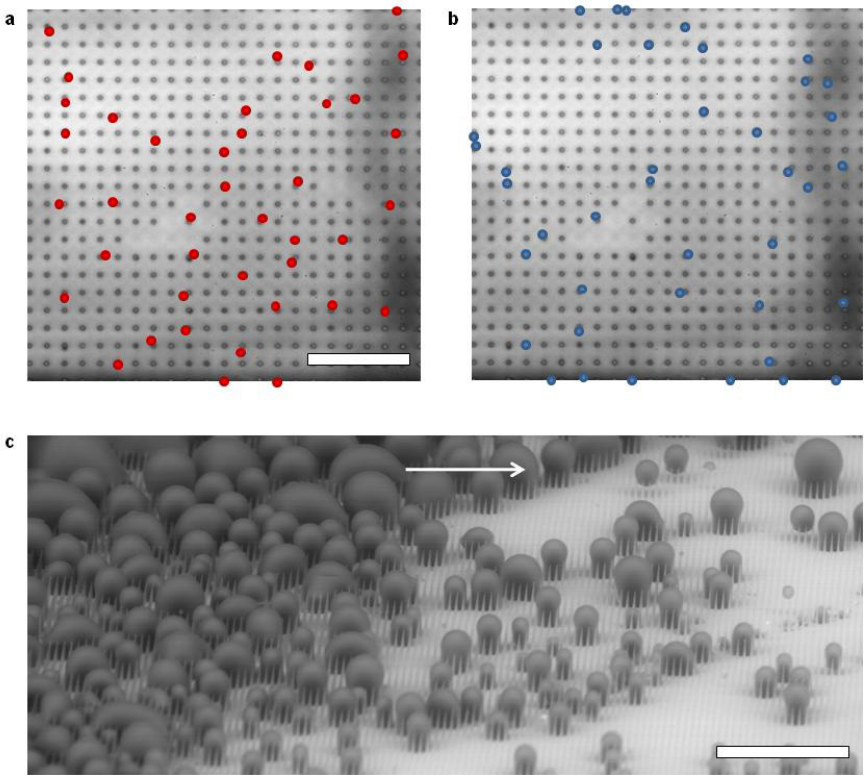

Supporting Figure S11.2 Nucleation behavior on SAM. Nucleation sites (indicated by dots) observed using OM at a fixed location on a structured silicon surface for two different CVD silane films, (a) C1 & (b) C2. The nucleation sites for each coating were observed to be repeatable over several repetitions of the nucleation process. Between runs the sample was held at $S \approx 0.15$ for 20 min to dry the sample. Nucleation conditions: $T_w = 283 \pm 0.1$ K, $S_{max} = 1.4 \pm 0.05$. Scale bar: 20 μm. (c) Comparison of nucleation density between an area of the surface subjected to prolonged electron beam exposure. The arrow indicates the panning direction to a previously unexposed region of the surface. The energy of the electron beam introduces defects into the silane coating significantly increasing the local nucleation density. Nucleation conditions: $T_w = 283 \pm 1.5$ K, $S_{max} = 1.07 \pm 0.11$. Scale bar: 80 μm.

Supplemental references

1. Kashchiev, D., *Nucleation: Basic Theory with Applications*. 1 ed.; Butterworth-Heinemann: Oxford, 2000.
2. Donald, A. M.; Stelmashenko, N. A.; Craven, J. P.; Terentjev, E. M.; Thiel, B. L., Topographic contrast of partially wetting water droplets in environmental scanning electron microscopy. *J Microsc-Oxford* 2001, 204, 172-183.
3. Young, T., An essay on the cohesion of fluids. *Philos. Trans. R. Soc. A* 1805, 95, 65.
4. Quéré, D., Wetting and Roughness. *Annual Review of Materials Research* 2008, 38, 71-99.
5. Oliver, J. F.; Huh, C.; Mason, S. G., Resistance to spreading of liquids by sharp edges. *J. Colloid Interface Sci.* 1977, 59, 568.
6. Tóth, T.; Ferraro, D.; Chiarello, E.; Pierno, M.; Mistura, G.; Bissacco, G.; Semprebon, C., Suspension of water droplets on individual pillars. *Langmuir* 2011, 27.
7. Du, J.; Michielsen, S.; Lee, H. J., Profiles of liquid drops at the tips of cylindrical fibers. *Langmuir* 2010, 26, 16000-16004.
8. Mayama, H.; Nonomura, Y., Theoretical considerations of wetting on a cylindrical pillar defect: Pinning energy and penetrating phenomena. *Langmuir* 2011, 27, 3550-3560.
9. Choi, W.; Tuteja, A.; Mabry, J. M.; Cohen, R. E.; McKinley, G. H., A modified Cassie-Baxter relationship to explain contact angle hysteresis and anisotropy on non-wetting textured surfaces. *J. Colloid Interface Sci.* 2009, 339, 208-216.
10. Patankar, N. A., Hysteresis with regard to Cassie and Wenzel states on superhydrophobic surfaces. *Langmuir* 2010, 26, 7498-7503.
11. Öner, D.; McCarthy, T. J., Ultrahydrophobic surfaces. Effects of topography length scales on wettability. *Langmuir* 2000, 16, 7777.
12. Kusumaatmaja, H.; Yeomans, J. M., Modeling contact angle hysteresis on chemically patterned and superhydrophobic surfaces. *Langmuir* 2007, 23, 6019.
13. Sbragaglia, M.; Peters, A. M.; Pirat, C.; Borkent, B. M.; Lammertink, R. G. H., Spontaneous breakdown of superhydrophobicity. *Phys. Rev. Lett.* 2007, 99, 156001.
14. Peters, A. M.; Pirat, C.; Sbragaglia, M.; Borkent, B. M.; Wessling, M.; Lohse, D.; Lammertink, R. G. H., Cassie-Baxter to Wenzel state wetting transition: Scaling of the front velocity. *Eur. Phy. J. E* 2009, 29, 391-397.
15. Pound, G. M.; Simnad, M. T.; Yang, L., Heterogeneous nucleation of crystals from vapor. *J. Chem. Phys.* 1954, 22.
16. Sigsbee, R. A., Adatom capture and growth rates of nuclei. *Journal of Applied Physics* 1971, 42, 3904-3915.
17. Pocker, D. J.; Hruska, S. J., Detailed calculations of the numberof distinct sites visited in random walk on several two-dimensional substrate lattices. *J. Vac. Sci. Tech.* 1971, 8, 700-707.
18. Hirth, J. P.; Pound, G. M., *Condensation and evaporation - nucleation and growth kinetics*. Pergamon Press: England, 1963.
19. Thiel, P. A.; Madey, T. E., The interaction of water with solid surfaces: Fundamental aspects. *Surface Science Reports* 1987, 7, 211-385.
20. Israelachvili, J. N., *Intermolecular and surface forces*. 2nd ed.; Academic Press: Amsterdam, 1991.
21. Ma, Y.; Foster, A. S.; Nieminen, R. M., Reactions and clustering of water with silica surface. *J. Chem. Phys.* 2005, 122.

22. Cao, P.; Xu, K.; Varghese, J. O.; Heath, J. R., The microscopic structure of adsorbed water on hydrophobic surfaces under ambient conditions. *Nano Lett.* 2011, dx.doi.org/10.1021/nl2036639.